

## Blood Flow in Small Curved Tubes

**C. Y. Wang**

Mem. ASME, Departments of Mathematics and  
Physiology, Michigan State University, East Lansing,  
MI 48824

**J. B. Bassingthwaite**

Center for Bioengineering, University of Washington,  
Seattle, WA 98195

*Blood flow in small curved tubes is modeled by the two-fluid model where a relatively cell-free fluid layer envelops a fluid core of higher viscosity. The parameters in the model are successfully curve fitted to experimental data for straight tubes. The curved tube equations are then solved by perturbation theory. It was found that curvature in general lowers the tube resistance, but increases the shear stress near the inside wall.*

[DOI: 10.1115/1.1634992]

### 1 Introduction

Blood can be considered as homogeneous in large blood vessels, but in small tubes the rheology shows considerable non-homogeneous behavior [1,2]. Due to the particulate nature of red blood cells, there is an almost cell-free layer of plasma near the vessel wall. The major effect of this layer is to decrease the apparent viscosity or resistance (the Fahraeus-Lindqvist effect), especially in medium to moderately small blood vessels. For vessels of 50-1000 microns, the phenomenon can be adequately described by the two-fluid model. First proposed by Vand [3] for general suspensions, the model assumes a homogeneous fluid core enclosed by a fluid annulus of lower viscosity. The two-fluid model has been applied to blood flow in straight tubes, notably by Hayes [4] and Sharan and Popel [5]. The theoretical derivation of the resistance formula of this model and our simple curve fit with blood flow data in small straight tubes are given in the Appendix.

In the microvasculature there are numerous instances where the blood vessels are curved or tortuous [6], especially in the diseased state. Also in biomechanical instrumentation blood may be transported through small curved tubes. It is the aim of this study to investigate the effect of curvature on the wall shear and the resistance of the flow through such a tube.

We shall use a coordinate system first proposed by Dean [7,8] to treat the flow in a circular tube of small constant curvature. The inertial effects are neglected since the Reynolds number in the

microcirculation is typically very small (of order  $10^{-3}$ ). The Dean number, proportional to (curvature)(Reynolds number)<sup>2</sup>, is even smaller. The secondary recirculation, which is prevalent for large curved tubes, would be entirely absent.

### Formulation

Let the tube be of radius  $a$ , with a constant centerline curvature  $K$ . An orthogonal system can then be constructed from the elemental distance squared (Fig. 1a):

$$|d\vec{x}|^2 = (dr)^2 + r^2(d\theta)^2 + L^2(ds)^2 \quad (1)$$

where the center line scale factor is

$$L \equiv 1 - Kr \cos \theta \quad (2)$$

$(r, \theta)$  are local polar coordinates and  $s$  is the coordinate along the center line. Since the inertial terms are absent, due to symmetry one can show only the velocity component  $w(r, \theta)$  in the  $s$  direction exists. Using the scale factors from Eq. (1) (e.g. Batchelor [9]) the Stokes equation reduces to:

$$\frac{\mu}{r} \left\{ \left[ \frac{r}{L} (Lw)_r \right]_r + \left[ \frac{1}{rL} (Lw)_\theta \right]_\theta \right\} = \frac{G}{L} \quad (3)$$

Here  $G$  is the constant center-line pressure gradient (assumed negative along  $s$ ), and  $\mu$  is the viscosity. Fig. 1b shows the two regions. Region *I* is the core containing red blood cells with velocity  $w_I$  and viscosity  $\mu_I$  and Region *II* is the cell-free layer of thickness  $t$  from the vessel wall and with velocity  $w_{II}$  and viscosity  $\mu_{II}$ . Eq. (3), with the same pressure gradient, is solved separately for the two regions. The boundary conditions are that on the axis (at  $r=0$ )  $w_I$  is bounded, on the wall (at  $r=a$ ) there is no slip, i.e.  $w_{II}(a, \theta) = 0$  and velocities and shear stresses match on the interface at  $r = a - t$ :

$$w_I = w_{II} \quad (4)$$

$$\mu_I L \left( \frac{w_I}{L} \right)_r = \mu_{II} L \left( \frac{w_{II}}{L} \right)_r \quad (5)$$

### Solution

The solution for the two-fluid flow in a straight circular tube is given in the Appendix. We shall perturb from this solution. Let the ratio of the tube radius to the radius of curvature of the center line be small, i.e.:

$$aK = \varepsilon \quad (6)$$

where  $\varepsilon \ll 1$ . (Actual values of  $\varepsilon$  is between 0 and 0.3 obtained from Ref. [6]). The other variable are normalized to order unity as follows:

$$\eta \equiv r/a \quad (7)$$

$$w_I = U(w_0 + \varepsilon w_1 + \varepsilon^2 w_2 + \dots) \quad (8)$$

$$w_{II} = \alpha U(u_0 + \varepsilon u_1 + \varepsilon^2 u_2 + \dots) \quad (9)$$

Contributed by the Bioengineering Division for publication in the JOURNAL OF BIOMECHANICAL ENGINEERING. Manuscript received by the Bioengineering Division September 5, 2002; revision received August 1, 2003. Associate Editor: A. D. Yoganathan.

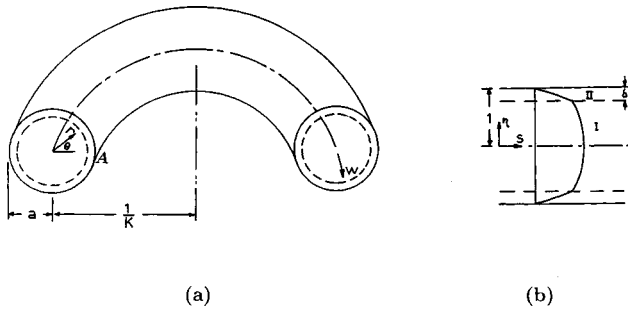


Fig. 1 (a) The curved tube coordinates  $(r, \theta, s)$ . The direction  $s$  is along the center line. (b) Axial cross section showing two fluid regions and the blunted velocity profile.

Here  $U = |G|a^2/4\mu_I$  is a normalized pressure gradient,  $\alpha \equiv \mu_I/\mu_{II}$ , and  $w_0, u_0$  is the normalized straight tube solution (Eqs. (A2-A4)):

$$w_0 = C - \eta^2, \quad u_0 = 1 - \eta^2 \quad (10)$$

where  $C$  is defined in Eq. (A4). Upon substitution of Eqs. (8,9) into Eqs. (3) the first-order equation is found to be

$$4\eta \cos \theta + \frac{1}{\eta} [\eta(w_1 - \eta w_0 \cos \theta)_{,\eta} + \eta^2 \cos \theta w_{0,\eta}]_{,\eta} + \frac{1}{\eta^2} (w_1 - \eta \cos \theta w_0)_{,\theta\theta} = 0 \quad (11)$$

The first-order equation for  $w_{II}$  is similar to Eq. (11), only with  $w$  replaced by  $u$ . Together with the perturbed boundary conditions Eqs. (4,5) the solution is:

$$w_1 = \cos \theta \left[ C_1 \eta - \frac{3}{4} \eta^3 \right] \quad (12)$$

$$u_1 = \cos \theta \left[ \frac{3}{4} (\eta - \eta^3) + C_2 \left( \eta - \frac{1}{\eta} \right) \right] \quad (13)$$

where  $\delta \equiv t/a$  and

$$C_1 = \frac{\{6 + (\alpha - 1)[18\delta - (16\alpha + 21)\delta^2 + (4\alpha + 3)(4\delta^3 - \delta^4)]\}}{4[2 + 2(\alpha - 1)\delta - (\alpha - 1)\delta^2]} \quad (14)$$

$$C_2 = \frac{7(\alpha - 1)\delta(2 - \delta)(1 - \delta)^2}{4[2 + 2(\alpha - 1)\delta - (\alpha - 1)\delta^2]} \quad (15)$$

Notice the outer region velocity  $u_1$  is zero on the tube wall but may include terms which are singular at the center. Since  $w_1, u_1$  are periodic in  $\theta$ , they do not contribute to the net flow rate, which is of higher order. However, for the second-order flow rate correction only the non-periodic part is needed.

Let an over bar denote the average with respect to the angle  $\theta$ . The averaging is then applied to the second-order terms of Eq. (3). The result is:

$$2\eta^3 - \left[ \eta \left( \frac{1}{2} \eta w_0 + \overline{\cos \theta w_1} - \overline{w_2} \eta \right) \right]_{,\eta} = 0 \quad (16)$$

with a similar equation for  $u_2$ . After some work, the solution is:

$$\bar{w}_2 = C_3 + \frac{C + C_1}{4} \eta^2 - \frac{11}{32} \eta^4 \quad (17)$$

$$\bar{u}_2 = -\frac{7 + 4C_2}{16} (1 - \eta^2) + \frac{11}{32} (1 - \eta^4) + C_4 \ln \eta \quad (18)$$

where

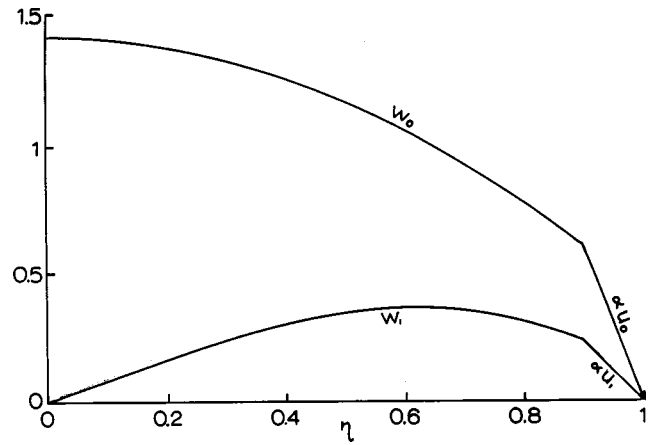


Fig. 2 Typical velocity profiles ( $\delta=0.1, \alpha=3.2, \theta=0$ ). The first-order correction  $w_1$  due to curvature is anti-symmetric.

$$C_3 = \frac{-1}{32[2 + 2(\alpha - 1)\delta - (\alpha - 1)\delta^2]} \times \{2 + (\alpha - 1)[10\delta + (8\alpha - 21)\delta^2 - 8(2\alpha - 3)\delta^3 + 2(7\alpha + 8)\delta^4 - 6(\alpha - 1)\delta^5 + (\alpha - 1)\delta^6 - 28\alpha\delta(2 - \delta)(1 - \delta)^2 \ln(1 - \delta)]\} \quad (19)$$

$$C_4 = \frac{21(\alpha - 1)(1 - \delta)^2 \delta(2 - \delta)}{8[2 + 2(\alpha - 1)\delta - (\alpha - 1)\delta^2]} \quad (20)$$

The net flow rate is then integrated

$$F = 2\pi a^2 U [q_0 + \varepsilon^2 q_2 + O(\varepsilon^4)] \quad (21)$$

where

$$q_0 = \int_0^{1-\delta} w_0 \eta d\eta + \alpha \int_{1-\delta}^1 u_0 \eta d\eta = \frac{\alpha}{4} \left[ 1 - (1 - \delta)^4 \left( 1 - \frac{1}{\alpha} \right) \right] \quad (22)$$

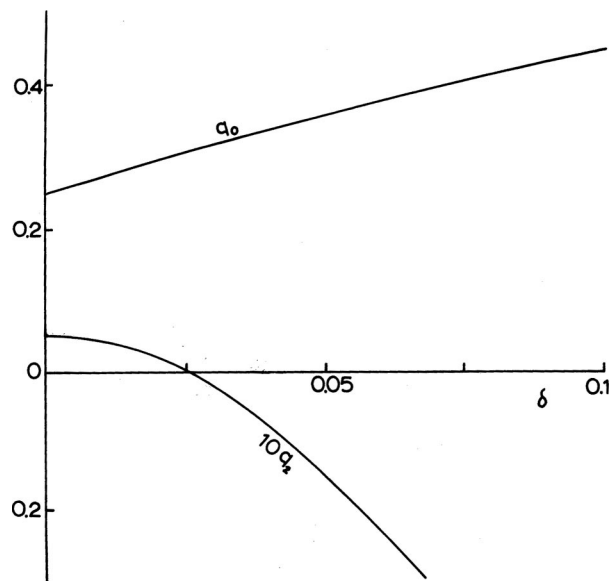


Fig. 3 The flow rate as a function of  $\delta$  ( $\alpha=3.317$ ).  $q_0$  is for the straight tube,  $q_2$  is the correction due to curvature.

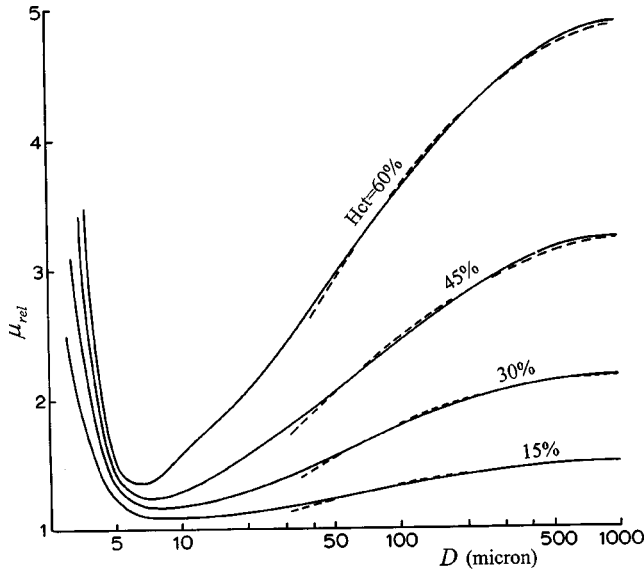


Fig. 4 Relative apparent viscosity as a function of diameter — glass tube experiments [10], --- Eq. (A8)

$$q_2 = \frac{\int_0^{1-\delta} \bar{w}_2 \eta d\eta + \alpha \int_{1-\delta}^1 \bar{u}_2 \eta d\eta}{1} = \frac{1}{192[2 + 2(\alpha-1)\delta - (\alpha-1)\delta^2]} \times \{2 + (\alpha-1)[14\delta - (576\alpha + 43)\delta^2 + 4(432\alpha + 19)\delta^3 - (1856\alpha + 85)\delta^4 + (832\alpha + 62)\delta^5 - (120\alpha + 29)\delta^6 - 8(\alpha-1)\delta^7 + (\alpha-1)\delta^8]\} \quad (23)$$

The above computations are facilitated by a computer program with symbolic capabilities

## Results and Discussions

Figure 2 shows some typical velocity distributions. The zeroth-order is a blunted parabola form which has been observed in experiments using straight tubes [2]. The first-order correction is due to the curving of the vessel. Contrary to high Reynolds number flows, the velocity near the inner surface is increased while that near the outer surface is decreased. Consequently the shear stress is higher on the inside wall near point A in Fig. 1a. The shear stress on the vessel wall is:

$$\tau = \mu_{II} w_{IIr} = \frac{|G|a}{4} (u_{0\eta} + \varepsilon u_{1\eta} + \dots) \Big|_{\eta=1} = \frac{|G|a}{4} \left[ -2 + \varepsilon \cos \theta \left( -\frac{3}{2} + \frac{7(\alpha-1)\delta(2-\delta)(1-\delta)^2}{2[2 + 2(\alpha-1)\delta - (\alpha-1)\delta^2]} \right) \right] \quad (24)$$

Whether higher local shear stress is the cause of vessel tortuosity is still uncertain at present. Fig. 3a shows a typical zeroth-order net flow rate  $q_0$  versus the thickness-radius ratio. For smaller vessels (larger  $\delta$ ) the flow rate can be as much as 50% more due to the lowered viscosity of the cell-free layer. Fig. 3b shows a typical first-order flow rate correction  $q_2$  due to curvature effects. Notice  $q_2$  becomes negative when  $\delta$  is larger than 0.026. This means the resistance of a larger curved vessel is lower than that of a straight vessel, but the resistance of a smaller curved vessel is higher than a straight vessel of the same size. These properties would persist even when the curvature is not small.

Table 1 Values of  $\alpha$  and  $t$  fitted to experimental data in Fig. 4.

$Hct$	15%	30%	45%	60%
$\alpha$	1.52	2.22	3.34	5.04
$t$	3.77	2.54	2.03	1.25

We can also solve Eq. (3) numerically. This is not recommended since the parameter  $\varepsilon$  is indeed small and the perturbation method is adequate. Furthermore perturbation solutions, being exact, do show more clearly the dependence of the various parameters.

## Appendix-Two-Fluid Flow in a Straight Tube

For a straight tube the curvature  $K$  is zero and thus the scale factor  $L = 1$ . Eq. (3) becomes the Poisson equation:

$$\frac{\mu}{r} \left[ (rw_r)_r + \frac{1}{r} w_{\theta\theta} \right] = G \quad (A1)$$

Let  $\delta \equiv t/a$  and  $\alpha \equiv \mu_I/\mu_{II}$ . The axisymmetric solution that satisfies the conditions of boundedness, no slip, and Eqs. (4,5) is:

$$w_I = \frac{|G|a^2}{4\mu_I} [C - (r/a)^2] \quad (A2)$$

$$w_{II} = \frac{|G|a^2}{4\mu_{II}} [1 - (r/a)^2] \quad (A3)$$

where

$$C = (1-\delta)^2 - \alpha[(1-\delta)^2 - 1] \quad (A4)$$

The total flow can be integrated

$$Q = \int_0^{a-t} w_I 2\pi r dr + \int_{a-t}^a w_{II} 2\pi r dr = \frac{\pi|G|a^4}{8\mu_{II}} \left[ 1 - (1-\delta)^4 \left( 1 - \frac{1}{\alpha} \right) \right] \quad (A5)$$

In order to compare with experiments, we define an apparent viscosity

$$\mu_{app} = \frac{\pi|G|D^4}{128Q} \quad (A6)$$

where  $D = 2a$  is the inside tube diameter, and a relative apparent viscosity

$$\mu_{rel} \equiv \frac{\mu_{app}}{\mu_{II}} \quad (A7)$$

Using Eq. (A5) we find

$$\mu_{rel} = \frac{1}{1 - (1-\delta)^4(1-1/\alpha)} \quad (A8)$$

This is essentially the result of Vand [3]. The apparent viscosity is that of the core when the thickness of the cell-free layer is zero, and is the plasma viscosity when the thickness equal the radius of the tube. Using in vitro experiments (in glass tubes) of 19 sources compiled by Pries et al. [1] and Secomb [10] we curve-fitted Eq. (A8) for each hematocrit as shown in Fig. 4. The fitted values of  $\alpha$  and  $t = D\delta/2$  are shown in Table 1.

The error of the curve fit is within 3% for diameter  $D$  from 40 to 1000 microns. We keep in mind that any shear dependence from rouleaux formation, cell deformation, rotation, wall effects, nonparticle free plasma layer, etc are included in the apparent

curve fit of the two parameters. Also included is the relation between the tube hematocrit and the feed hematocrit, upon which the data was based. Thus it is not necessary to consider such complicated effects for the two-fluid model. For in vivo experiments with blood vessels instead of glass tube, the experiments show higher apparent viscosity, probably due to the uneven glycocalyx wall. The curves however can be fitted similarly.

## Acknowledgment

This research is partially supported by NIH Grant RR 01243.

## References

- [1] Pries, A. R., Secomb, T. W., Gaetgens, P., 1966, "Biophysical Aspects of Blood Flow in the Microvasculature," *Cardiovasc. Res.*, **32**, pp. 654–667.
- [2] Bishop, J. J., Popel, A. S., Intaglietta, M., Johnson, P. C., 2001, "Rheological Effects of Red Blood Cell Aggregation in the Venous Network: A Review of Recent Studies," *Biorheology*, **38**, pp. 263–274.
- [3] Vand, V., 1948, "Viscosity of Solutions and Suspensions I Theory," *J. Phys. Chem.-US*, **52**, pp. 277–299.
- [4] Hayes, R. H., 1960, "Physical Basis of the Dependence of Blood Viscosity on Tube Radius," *Am. J. Physiol.*, **198**, pp. 1193–1200.
- [5] Sharan, M., and Popel, A. S., 2001, "A Two-Phase Model for Flow of Blood in Narrow Tubes With Increased Effective Viscosity Near the Wall," *Biorheology*, **38**, pp. 415–428.
- [6] Nicola, P. D., Maggi, G., and Tassi, G., 1983, *Microcirculation-An Atlas*, Schattauer, Stuttgart.
- [7] Dean, W. R., 1927, "Note on the Motion of a Fluid in a Curved Pipe," *Phil. Mag. Ser. 7*, **4**, pp. 208–233.
- [8] Berger, S. A., Talbot, L., and Yao, L. S., 1983, "Flow in Curved Pipes," *Annu. Rev. Fluid Mech.*, **15**, pp. 461–512.
- [9] Batchelor, G. K., 1967, *An Introduction to Fluid Dynamics*, Cambridge Univ. Press Appendix 2.
- [10] Secomb, T. W., 1995, "Mechanics of Blood Flow in the Microcirculation," in *Biological Fluid Dynamics*, C. P. Ellington and T. J. Pedley Eds. Soc. Exp. Biol., Cambridge, MA pp. 305–321.

## A Novel Device to Evaluate the Stiffness of Ankle-Foot Orthosis Devices

P. Cappa,<sup>1,2</sup> F. Patanè,<sup>1</sup> and M. M. Pierro<sup>3</sup>

<sup>1</sup>Department of Mechanics and Aeronautics, University of Rome "La Sapienza," Via Eudossiana 18, Rome, Italy <sup>2</sup>Clinical Engineering Service, Children's Hospital "Bambino Gesù," Piazza San Onofrio, 4, Rome, Italy <sup>3</sup>Paediatric Neuro-Rehabilitation Division, Children's Hospital "Bambino Gesù," Palidoro, Rome, Italy

*The evaluation of mechanical behavior of plastic Ankle-Foot Orthosis (AFO) is important since AFO can provide an efficient support to patients with disabilities in locomotion. This paper reports on a novel testing apparatus that allows: (a) the evaluation of AFO stiffness in sagittal and frontal planes; (b) the conduction of semi-automatic trials; and, finally, (c) a global accuracy associated to the AFO stiffness values always less than 4%. The stiffness values are determined by the measurements of the imposed relative displacements between the foot and the shank of the orthosis and the induced reaction forces. The data collected together in an exact 2-D approach, together with those provided by gait analysis systems, allows to better understand gait alteration induced by ankle orthosis, and to improve clinical management of patients. [DOI: 10.1115/1.1634993]*

## Introduction

Orthotic devices for lower limb assistance, such as unarticulated AFO (Ankle-Foot Orthosis), are orthotic appliances capable of providing sufficient support for the lower leg to maintain an upright position and are commonly prescribed for hemiplegics to control excessive plantar flexion to improve gait [1,2].

Even though it is clear that AFOs dynamically interfere with the gait kinematics, acting as complex springs coupled in parallel with the ankle dorsi/plantar-flexors, it is still unknown how the mechanical properties of AFOs should be selected in relation to the particular pathology of patients. Studies conducted were focused on the impact of different AFO configurations on the function of locomotion in patients affected by hemiplegia [3–5]. As a general observation, the purpose of studies conducted in that field was to objectively evaluate the effects of specific AFO design on gait function of pathological and healthy subjects, depending on a global comparison of results obtained with healthy patients and data collected while the patients walk wearing the orthosis, shoes or barefoot. The aim was to identify the best among some other orthotic devices usually prescribed in clinical practice. However, the tests conducted did not permit the correlation of AFO geometry and material properties directly to gait modifications in order to find some indication on the design of AFO. These indications could be: (a) the realization of novel improved ad hoc design or (b) a proper modification by trimming an existing manufactured AFO. The tasks mentioned can be reached only by putting in relation: (a) the dynamic structural properties of the AFO with (b) the consequent patient gait modifications. Since point (b) is measurable directly by means of optoelectronic systems, point (a) should also be quantified by means of an adequate testing device. Hence, AFO stiffness can be considered the most important mechanical property, because AFO interferes with the muscular action in a spring-like mode. Since it is commonly accepted in motor control behavior that a continuous and adaptive variation appears in the relative stiffness [6–10] of agonist and antagonist muscles, the AFO adds its stiffness directly to the muscular one.

Moreover, in the literature some researches were conducted in evaluating numerically or experimentally the stiffness or the flexibility of AFOs. The flexibility was initially examined numerically [11–18] with the principal aim of preventing failure due to the effect of fatigue. Other scientific papers were devoted to the experimental validation of the state of stress obtained numerically and the results generally confirmed both the findings from FEA and the observed failures in clinical practice [14] and [19–21]. Other papers are available in the literature and are more generally focused on the experimental evaluation of the stiffness of AFOs carried out by means of simple mechanical devices. Such devices lack in the evaluation of the stiffness of AFOs by means of 1-D or pseudo-2-D approach and generally have determined the stiffness values only in two fixed directions [22–25]. An apparatus, capable of partially overcoming the mentioned limitations, was proposed by Klasson et al. [26]; that device detected the flexibility of an AFO in 5 degrees-of-freedom (DOF) however, because the displacement transducers were read sequentially, the proposed method was sensitive to the creep of the plastic.

Finally, some researchers have suggested that stiffness measurement of the AFOs may be carried out by means of an optoelectronic system [27]. However, the viability of the proposed experimental methodology suffers when numerous AFOs have to be examined and largely depends on the skill of the experimentalist.

Corresponding author: University of Rome "La Sapienza," Via Eudossiana, 18; 00184 Roma, Italy. Phone: ++39-06-44585273; Fax: ++39-06-4881759 e-mail: paolo.cappa@uniroma1.it.

Contributed by the Bioengineering Division for publication in the JOURNAL OF BIOMECHANICAL ENGINEERING. Manuscript received by the Bioengineering Division October 21, 2002; final revision received May 6, 2003. Associate Editor: K. Vaughan.

The main task, in the present research project, is the development of an orthosis test apparatus capable of accomplishing the following requirements, in determining the data of AFO stiffness: (a) results are synthesized in reports comparable with other results made available by the gait analysis systems; (b) the global inaccuracy must be less than about  $\pm 5\%$ ; and, finally, (c) should have a low-cost design. The previously indicated range of variation of inaccuracy is justified by considering that the manufacturing process does not allow better repeatability in nominally identical AFOs.

## Methods

**1.1 General Project Description.** The structural testing machine to be designed and built must perform, at the present stage of the research project, tests on plastic AFOs in a manually operated manner. However, it should also be possible to upgrade the system without much difficulty to a closed loop system so that an entire test could be performed automatically. The test apparatus is designed to enable known relative movements of the foot, in respect to the shank, applied by the experimenter. The resulting moments are then evaluated by means of an on-line post-processing of the measured interaction forces that are exerted between the rigid frame of the testing device and the AFO. Hence, the testing machine should be instrumented to evaluate the displacement of the shank referred to the foot imposed by the operator (i.e., the applied input) and to measure the consequent interaction force (i.e., the obtained output). From the two sets of variables, the stiffness can then be calculated.

We chose the joint coordinate system [28–30] and the Cardan angle sequence ( $\alpha, \beta, \gamma \Rightarrow x, y, z$  axis rotation sequence) to describe the relative position of the foot in respect to the shank. Moreover, at the present stage, the analysis was focused on the two anatomic reference planes that are generally of interest: the sagittal and frontal planes. Our choice would also ensure that the representativeness of data collected, would not be compromised even though the variables relative to the third dimension, i.e., the transverse plane, would not be monitored at the present phase. The scheme of the force-testing machine must take into account fund constraints.

**1.2 Design and Theoretical Consideration.** The force-testing machine was realized, basically, by assembling off-the-shelf mechanical elements and is a screw type, see Fig. 1. The main components are: a cross table with two  $x/y$  hand-controlled slides and a tough frame used for vertical drill. The key point is the interaction force between the rigid frame and the AFO that, due to the 3-D nature of the test, requires the use of an expensive six-component load cell. To avoid the use of such a component, the mechanical connection between the AFO and the testing system was designed to decouple and reduce the number of force components to be measured.

The foot model is firmly connected to the fixed and rigid frame and joined to the shank by means of a prismatic and a cardanic joint as shown in Fig. 1; then, the operator can slide Frame 1 along  $x$  and  $y$  directions by a cross table in order to move the shank only. Due to the design choice, the following equations (Appendix I) can be obtained that express the relations among: (a) shank attitude; (b) position of the moving point  $O_1$ ; and (c) distance  $L$  between the initial reference point  ${}^0O_1$  and its generic position  $O_1$ :

$$x = L \frac{\tan(\alpha)}{\cos(\beta)}; \quad y = L \tan(\beta) \quad (1)$$

It can be shown that if the operator moves at first point  $O_1$  to a  $y$  arbitrary position, the ab/adduction angle  $\beta$  is locked and known, then, holding the  $y$  value, simply by sliding point  $O_1$  into direction  $x$  only the dorsi-plantar flexion angle  $\alpha$  can change. It is necessary to note that the design proposed is able to decouple rotation  $\gamma$  to the monitored variables  $x$  and  $y$ , and, consequently, also to the

calculated values  $\alpha$  and  $\beta$ . In order to determine the moment in the sagittal and in the frontal planes ( $M_\alpha$  and  $M_\beta$ ), it is sufficient to measure the components of reaction force in direction  $x$  and  $y$  (Appendix I):

$$\begin{bmatrix} M_\alpha \\ M_\beta \end{bmatrix} = {}^1J_4^T {}^1F = \begin{bmatrix} -F_x \frac{L}{\cos^2(\alpha)\cos(\beta)} \\ \frac{L}{\cos^2(\beta)} (F_y - F_x \tan(\alpha)\sin(\beta)) \end{bmatrix} \quad (2)$$

Where:

$${}^1J_4 = \begin{bmatrix} \frac{\partial {}^1O_4}{\partial \alpha} & \frac{\partial {}^1O_4}{\partial \beta} \end{bmatrix} \quad (3)$$

Finally, AFO stiffness  $K$  is a function of both the angles  $\alpha$  and  $\beta$ , and is defined by:

$$K(\alpha, \beta) = \begin{pmatrix} \frac{\partial M_\alpha}{\partial \alpha} & \frac{\partial M_\alpha}{\partial \beta} \\ \frac{\partial M_\beta}{\partial \alpha} & \frac{\partial M_\beta}{\partial \beta} \end{pmatrix} \quad (4)$$

**1.3 Experimental Set-up and Testing Procedure.** The bone model of shank is a prismatic slider and it is inserted into a rigid plastic one modeled so that it adheres to the AFO examined. The foot model only consists of a rigid metal plate that adheres to the sole of the AFO and it is connected to frame 0 via two small holes. It should be noted that the present study fails, at the current stage, to represent of the orthoses/tissue interface and makes no allowance for compliant feet. It is worth noting that such a choice was also made in other experimental researches and it is, in our opinion, the necessary procedure for an exhaustive evaluation of mechanical properties of AFOs. In fact, a rigid shank model permits the understanding of the correlation between an AFO deflection and its consequent reaction moments while the compliance of the soft tissue actually belongs to the patient's behavior.

To conduct the test, a spiral AFO is fitted to the foot-shank surrogate and the "knee position," point  $O_4$  of Fig. 1, is connected to the base plate of the moving frame via a cardanic joint. The position of the  $x/y$  slider screws is monitored by two rotary incremental optical encoders, while the induced reaction of the AFO is evaluated by means of the measurement of  $F_x$  and  $F_y$  at point  $O_1$ , by two single-axis load cells with the sensing axis located on the table plane. In this way, the proposed testing machine design allows the evaluation of force vector by the use of a multi-components sensor made up of two unidirectional sensors connected to the rigid frame by means of *ad hoc* decoupling zones. Such a choice reduces the cost of the experimental set-up significantly. However, both the misalignment effects and the axial clearance of the linear guide to which the load cells are connected could determine inefficient decoupling zones, hence a verification procedure was adopted. The verification system of the spurious element magnitude consists of a force generation system, i.e., a dead weight and a wire, that transmit a force in a known direction applied at loading point  $O_1$ . A weight of 29.4 N was chosen, the multi-components sensor was tested three times and the raw data was interpolated with a least square method. The differences observed, described in the following, are: (a) a standard deviation of the vector magnitude always less than 2 N and (b) a maximum error associated to the planar angle, i.e., the projection of the force vector in the  $x/y$  reference plane, of  $5^\circ$ .

A multifunction data acquisition unit (16 bit) was used to acquire 100 force signal data points every 1 mm traveled by the cross table in  $x$  direction and 5 mm in  $y$  direction. Four runs were imposed in  $x$  direction leaving  $y$  fixed, consequently for each AFO attitude four displacement and load data were gathered.

At the present stage of the research project, it was decided to zero  $M_\gamma$ , i.e., ext/internal rotation moment, leaving the foot free

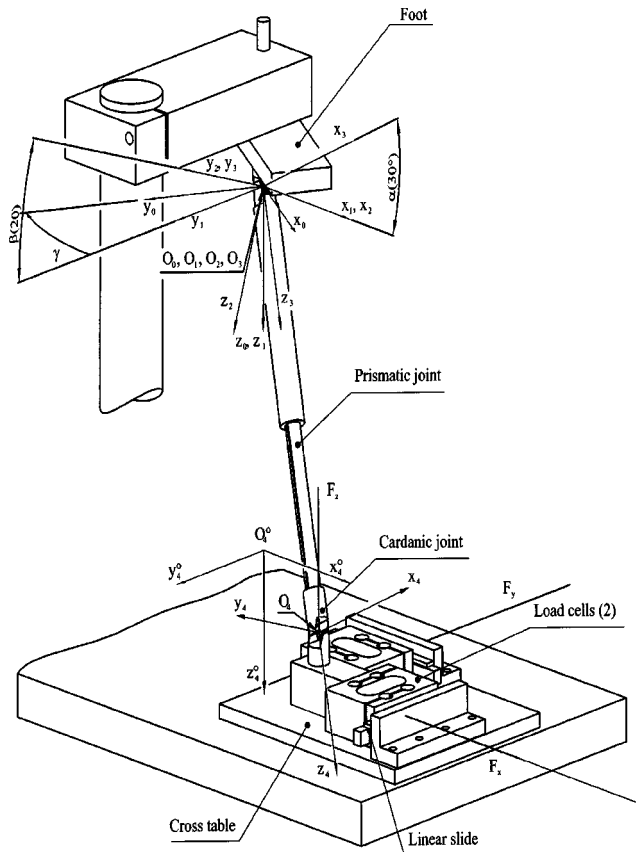


**Fig. 1** Scheme of the AFO testing machine: two elementary rotation of abduction and flexion are represented here by angles  $\beta < 0$  and  $\alpha < 0$  respectively,  ${}^0O_1$  is the “neutral” position of the “knee”; the rotation  $\gamma$  is also showed.

to rotate with respect to the shank and not to monitor  $\gamma$ , i.e., ext/internal rotation angle. However, imposing in the experimental protocol  $M_\gamma = 0$ , does not represent a significant limitation, because the patient’s shank can transmit to the internal surface of an AFO only shear values that determine small ext/internal rotation moment.

In order to calculate the uncertainties relative to  $\alpha$  and  $\beta$ ;  $M_\alpha$  and  $M_\beta$ ; and  $K$ , the usual propagation theory was used. It was hypothesized that the errors are independent and symmetrical with regard to positive and negative values, so the method of adding in quadrature was adopted. The uncertainty associated with angles and moments can be estimated, from a conservative point of view, by considering the geometrical condition most favorable for the measurement and by extending it to the whole set of measures. Hence, for geometrical reasons, the worst condition for the measurement of angles and moments occurs when both  $\alpha$  and  $\beta$  are equal to 0. As the uncertainties associated with: (a)  $x$  and  $y$  are  $\approx 0.5$  mm, mainly due to slider backlash; (b)  $L$  is  $\approx 1$  mm, due to operator skill; and (c)  $F_x$  and  $F_y$  are  $\approx 1$  N, by manipulating Eqs. 1 and 2 results:  $\varepsilon_{\alpha/\beta} \approx 1\%$ ,  $\varepsilon_{M_\alpha/M_\beta} \approx 3.4\%$ , and  $\varepsilon_{K_\alpha/K_\beta} \approx 4\%$ .

## Results and Discussion

All the data collected are synthesized in Fig. 2, where the total ankle moment  $M_t = \sqrt{M_\alpha^2 + M_\beta^2 + M_\gamma^2} = \sqrt{M_\alpha^2 + M_\beta^2}$  is represented as a function of  $\alpha$  and  $\beta$ . By examining the isolevel curves, the non-symmetric behavior of the tested AFO is clearly evident; such statement is consistent with the results available in literature. The observation can be summarized by two indicators: the characteristic angles of the maximum and minimum stiffness of the AFO, that are also indicated in the figure. In our opinion, the two angles

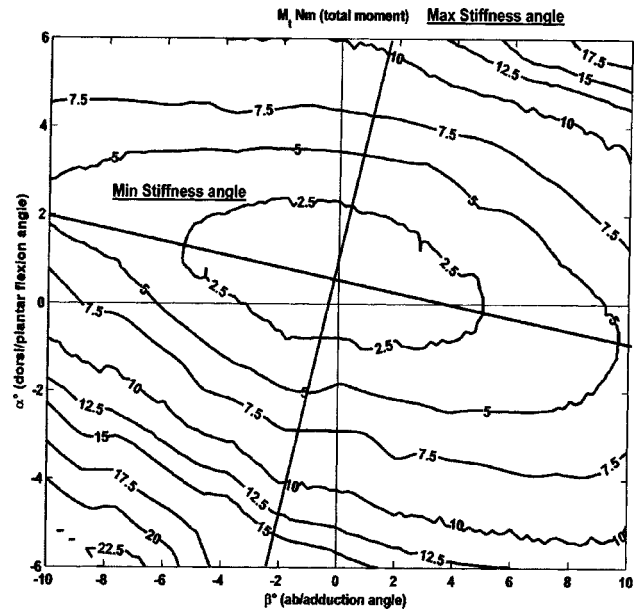


**Fig. 2** Variation of the total moment  $\sqrt{M_\alpha^2 + M_\beta^2 + M_\gamma^2}$  as a function of  $\alpha$  and  $\beta$ . The moment  $M_\gamma$  is always zeroed because the foot is free to rotate.

could synthetically represent mechanical behavior of the generic spiral AFO. However, Fig. 2 also provides an indication of the non-linear relationship between the total moment and the imposed angles  $\alpha$  and  $\beta$ .

Thus, to examine the mechanical behavior of the orthosis in greater detail, the data may be rearranged in a different manner to emphasize the non-constant and also non-linear relationship between the stiffness and the attitude of the AFO. Hence, the following synthetic indexes of the orthosis stiffness,  $K_\alpha$  and  $K_\beta$ , could be introduced:

$$K_\alpha = K(\alpha, \beta) = \frac{\partial M_\beta}{\partial \beta}(\alpha, \beta) \quad (5)$$

$$K_\beta = K(\alpha, \beta) = \frac{\partial M_\alpha}{\partial \alpha}(\alpha, \beta) \quad (6)$$

The reason for introducing the above mentioned indexes, instead of analyzing the full stiffness function  $K(\alpha, \beta)$  is that they represent a synthesis of the biomechanical behavior of the AFO. The methodology adopted to calculate stiffness  $K_\alpha$  and  $K_\beta$  evidently introduced some approximations because of the averaging effects, but it is conversely capable of synthetically visualizing and quantifying the non-linear behavior of spiral AFOs.

Both stiffness indexes  $K_\alpha$  and  $K_\beta$  were fitted with the two quadratic functions indicated in Fig. 3. The validity of the fit gave in both the cases an  $R_{adj}^2$  always greater than 0.95. The distribution observed is consistent with expected theoretical distribution with a confidence level set to 95% by  $\chi^2$  test. From an examination of those graphs the significant non-linear mechanical behavior of the examined spiral AFO emerges clearly.

By means of the experimental procedure adopted a quantitative evaluation of AFOs elastic properties is made available to the medical staff, who can then prescribe the more appropriate orthotic device for a patient, starting from its actual elastic properties, while, in current practice that choice is based on visual analysis of the geometry of AFOs or on suggestions by the manufacturers.

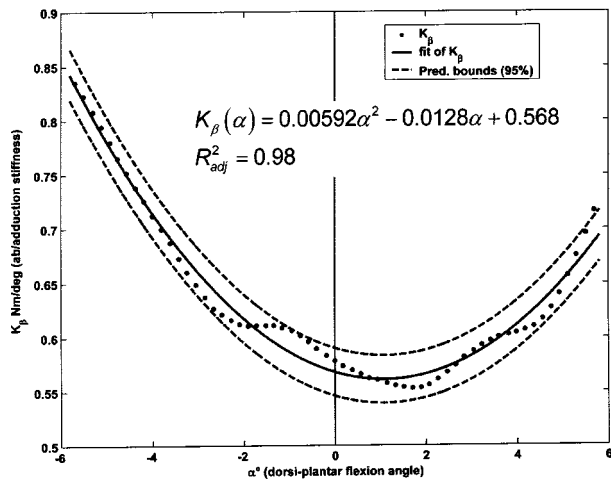
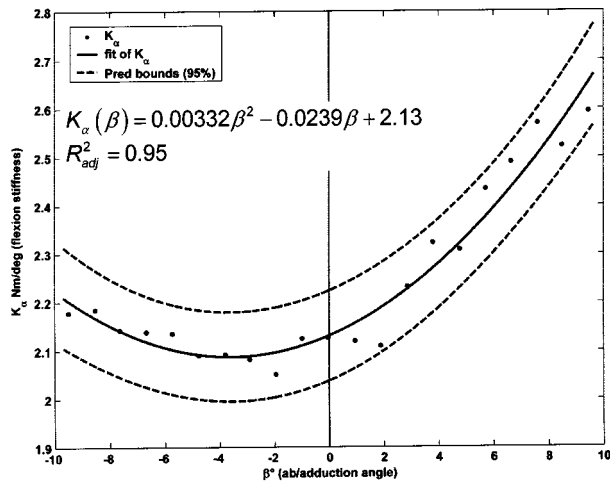


Fig. 3 (a) Variation of the average stiffness  $K_\alpha$  (averaged between  $-6^\circ$  and  $6^\circ$ ) as a function of  $\beta$ ; (b) variation of the average stiffness  $K_\beta$  (averaged between  $-10^\circ$  and  $10^\circ$ ) as a function of  $\alpha$ .

### Conclusions

The potential of the proposed testing machine to successfully perform tests on AFOs has been demonstrated. Hence, the target to craft a test system so that it delivers valid data in a form that the user can easily assimilate is reached. The stiffness graphs here proposed can be inserted effectively in the AFO data sheet to complete the information made available to the user.

Consequently, the test apparatus could permit in perspective a procedure capable of tailoring the AFO to the needs of a specific patient to obtain moderate or large ankle movements and evaluating the mechanical behavior of future design of AFOs prior to the clinical trial. The proposed apparatus can be upgraded by using a motorized slider to conduct not only quasi-static trials, but also dynamic ones, so that the tests are even closer to the actual use of AFOs.

### Nomenclature

- $F_x, F_y$  = forces measured by the  $x$  and  $y$  load cells
- ${}^jH_i$  = roto-translation homogeneous matrix from frame  $j$  to frame  $i$
- $K_\alpha$  = is the stiffness as a function of  $\alpha$  obtained by averaging in a chosen  $\beta$  range,
- $K_\beta$  = is the stiffness as a function of  $\beta$  obtained by averaging in a chosen  $\alpha$  range.

- $L$  = vertical (constant) distance between origins  $O_3-O_4$
- $M_\alpha, M_\beta, M_\gamma$  = dorsi/plantar flexion, ab/adduction, ext/internal rotation moments
- $O_i$  = origin of frame  $i$
- ${}^jP_i$  = point  $P_i$  respect to frame  $j$
- $S$  = multicomponent load cell sensitivity ( $2 \times 2$ ) matrix
- $x, y$  = cross-plate displacements
- $\alpha, \beta, \gamma$  = dorsi/plantar flexion, ab/adduction, ext/internal rotation angles
- $\varepsilon_{\alpha/\beta}$  = uncertainties relative to  $\alpha, \beta$  angles
- $\varepsilon_{x/y}$  = uncertainties relative to  $x, y$  displacements
- $\varepsilon_{M_\alpha/M_\beta}$  = uncertainties relative to  $M_\alpha$  and  $M_\beta$  moments
- $\varepsilon_{K_\alpha/K_\beta}$  = uncertainties relative to  $K_\alpha$  and  $K_\beta$  Stiffness

### Appendix I

The configuration of the mechanical system {foot}/(ankle joint)/(shank) i.e. {frame 0}/(frames 1-2-3)/(frame 4) is determined by its roto-translation homogeneous matrices

$$\begin{aligned}
 & {}^0H_1, {}^1H_2, {}^2H_3, {}^3H_4: \\
 & {}^0H_1 = \begin{bmatrix} c_\gamma & s_\gamma & 0 & 0 \\ -s_\gamma & c_\gamma & 0 & 0 \\ 0 & 0 & 1 & 0 \\ 0 & 0 & 0 & 1 \end{bmatrix}, \quad {}^1H_2 = \begin{bmatrix} 1 & 0 & 0 & 0 \\ 0 & c_\beta & s_\beta & 0 \\ 0 & -s_\beta & c_\beta & 0 \\ 0 & 0 & 0 & 1 \end{bmatrix} \\
 & {}^2H_3 = \begin{bmatrix} c_\alpha & 0 & s_\alpha & 0 \\ 0 & 1 & 0 & 0 \\ -s_\alpha & 0 & c_\alpha & 0 \\ 0 & 0 & 0 & 1 \end{bmatrix} \\
 & {}^3H_4 = \begin{bmatrix} 1 & 0 & 0 & 0 \\ 0 & 1 & 0 & 0 \\ 0 & 0 & 1 & l \\ 0 & 0 & 0 & 1 \end{bmatrix} = \begin{bmatrix} 1 & 0 & 0 & 0 \\ 0 & 1 & 0 & 0 \\ 0 & 0 & 1 & L \frac{1}{c_\alpha c_\beta} \\ 0 & 0 & 0 & 1 \end{bmatrix}, \quad \text{with} \\
 & L = l \cdot c_\alpha c_\beta.
 \end{aligned}$$

To obtain  $\alpha, \beta$  as a function of the measured values  $x, y$  it must be imposed

$$\begin{aligned}
 & \begin{bmatrix} 1 & 0 \\ 0 & 1 \end{bmatrix} {}^1O_4 = {}^1H_4 \begin{bmatrix} 4 & 0 \\ 0 & 1 \end{bmatrix} O_4, \quad \text{with} \\
 & {}^1H_4 = {}^1H_2 \cdot {}^2H_3 \cdot {}^3H_4 = \begin{bmatrix} c_\alpha & 0 & -s_\alpha & -L \frac{t_\alpha}{c_\beta} \\ s_\alpha s_\beta & c_\beta & c_\alpha s_\beta & L \cdot t_\beta \\ c_\beta s_\alpha & -s_\beta & c_\alpha c_\beta & L \\ 0 & 0 & 0 & 1 \end{bmatrix}, \\
 & {}^1O_4 = \begin{bmatrix} x \\ y \\ L \end{bmatrix}, \quad {}^4O_4 = \begin{bmatrix} 0 \\ 0 \\ 0 \end{bmatrix}.
 \end{aligned}$$

The solution is:

$$\begin{bmatrix} 1 & 0 \\ 0 & 1 \end{bmatrix} {}^1O_4 = {}^1H_4 \begin{bmatrix} 4 & 0 \\ 0 & 1 \end{bmatrix} O_4 \begin{cases} \beta = \text{atan}(y/L) \\ \alpha = \text{atan}\left(\frac{x/L}{\sqrt{1+(y/L)^2}}\right) \end{cases}$$

The measured valued of forces at the load cell plane are

$${}^1F = \begin{bmatrix} F_x \\ F_y \\ F_z \end{bmatrix} = \begin{bmatrix} S^{-1} \begin{bmatrix} V_1 \\ V_2 \end{bmatrix} \\ F_z \end{bmatrix},$$

and to obtain the moments  $M_\alpha, M_\beta$  we can calculate the Jacobian  ${}^1J_4 = [\partial^1 O_4 / \partial \alpha, \partial^1 O_4 / \partial \beta]$ :

$$\begin{bmatrix} M_\alpha \\ M_\beta \end{bmatrix} = {}^1J_4^T F = \begin{bmatrix} -F_x \frac{L}{c_\alpha^2 c_\beta} \\ \frac{L}{c_\beta^2} (F_y - F_x t_\alpha s_\beta) \end{bmatrix}$$

## References

- [1] Mollan, R. B., and James, W. V. A., 1977, "New flexible design of drop-foot orthosis," *Injury*, **8**(4), pp. 310–314.
- [2] Lehmann, J. F., Condon, S. M., Price, R., and de Lateur, B. J., 1987, "Gait abnormalities in hemiplegia: their correction by ankle-foot orthosis," *Arch. Phys. Med. Rehabil.*, **68**, pp. 763–771.
- [3] Romkes, J., and Brunner, R., 2002, "Comparison of a dynamic and a hinged ankle-foot orthosis by gait analysis in patients with hemiplegic cerebral palsy," *Gait & Posture*, **15**, pp. 18–24.
- [4] Nahorniak, M. T., Gorton, III, G. E., Gannotti, M. E., and Masso, P. D., 1999, "Kinematic compensations as children reciprocally ascend and descend stairs with unilateral and bilateral solid AFOs," *Gait & Posture*, **9**, pp. 199–206.
- [5] Thomas, S. S., Buckon, C. E., Jakobson-Huston, S., Sussman, M. D., and Aiona, M. D., 2002, "Stair locomotion in children with spastic hemiplegia: the impact of three different ankle foot orthosis (AFOs) configurations," *Gait & Posture*, **16**, pp. 180–187.
- [6] Duan, X. H., Allen, R. H., and Sun, J. Q., 1997, "A stiffness-varying model of the human gait," *Med. Eng. Phys.*, **19**, pp. 518–524.
- [7] Davis, R. B., and De Luca, P. A., 1996, "Gait characterization via dynamic joint stiffness," *Gait & Posture*, **4**, pp. 224–231.
- [8] Winter, D. A., Patla, A. E., Prince, F., Ishac, M., and Gielo-Perczak, K., 1998, "Stiffness control of balance in quiet standing," *J. Neurophysiol.*, **80**(3), pp. 1211–1221.
- [9] Morasso, P. G., and Schieppati, M., 1999, "Can muscle stiffness alone stabilize upright standing?," *J. Neurophysiol.*, **82**(3), pp. 1622–1626.
- [10] Winter, D. A., Patla, A. E., Rietdyk, S., and Ishac, M. G., 2001, "Ankle muscle stiffness in the control of balance during quiet standing," *J. Neurophysiol.*, **85**(6), pp. 2630–2633.
- [11] Leone, D., Diemente, S., Gustave, S., Lopez, I., 1998, "Structural analysis of solid ankle-foot orthosis," *Bioengineering Conference Proceedings of the 1988 Fourteenth Annual Northeast*, pp. 26–28.
- [12] Leone, D., 1987, "A structural model for molded thermoplastic ankle-foot Orthosis analysis," *J. Biomech. Eng.*, **109**, pp. 305–310.
- [13] Leone D., Diemente, S., Lopez-Isa, M., 1991, "Structural stability prediction for thermoplastic ankle-foot orthosis," *Bioengineering Conference, Proceedings of the 1991 IEEE Seventeenth Annual Northeast*, pp. 231–232.
- [14] Chu, T., 1995, "Experimental validation on finite element stress analysis of a polymeric orthotic device," *IEEE-EMBC and CMBC*, **2**, pp. 1259–1260.
- [15] Deitz, D., 1997, "Optimizing orthotic designs with FEA," *Mechanical Engineering Magazine* July issue, **119**(7), pp. 70–71.
- [16] Chu, T. M., Reddy, N. P., and Padovan, J., 1995, "Three dimensional finite element stress analysis of the polypropylene, ankle foot orthosis static analysis," *Med. Eng. Phys.*, **17**, pp. 372–9.
- [17] Reddy, N. P., Pohit, G., Lam, P. C., Grotz, R. C., 1985, "Finite element modelling of ankle-foot orthoses," *Proc Inter Conf Biomechanics and Clinical Kinesiology of Hand and Foot*, Indian Institute of Technology, pp. 97–99
- [18] Syngellakis, S., Arnold, M. A., and Rassoulian, H., 2000, "Assessment of the nonlinear behaviour of plastic ankle foot orthoses by the finite element method," *Proc. Inst. Mech. Eng.*, **214**(5), pp. 527–539.
- [19] Chu, T., Reddy, N. P., and Padovan, J., 1995, "Stress Distribution in the Ankle-Foot Orthosis Used to Correct Pathological Gait," *J. Rehabil. Res. Dev.*, **32**(4), pp. 349–360.
- [20] Chu, T., and Chu, T., 1996, "A Bonding Methods of Strain Gages to the Polypropylene Ankle-Foot Orthosis," *Exp. Tech.*, **20**(5), pp. 29–31.
- [21] Chu, T., 2000, "Determination of peak stress on polypropylene ankle-foot orthoses due to weight change using strain gage technology," *Exp. Tech.*, **24**(2), pp. 28–30.
- [22] Yamamoto, S., Ebina, M., Iwasaki, M., Kubo, S., Kawai, H., and Kawai, H., 1993, "Comparative Study of Mechanical Characteristics of Plastic AFOs," *J of Prosthetics and Orthotics*, **5**, pp. 259–264.
- [23] Lunsford, T. R., Ramm, T., and Miller, J., 1994, "Viscoelastic Properties of Plastic Paediatric AFOs," *J of Prosthetics and Orthotics*, **6**, pp. 3–9.
- [24] Singerman, R., Hoy, D. J., Mansour, J., 1999, "Design Changes in Ankle-Foot Orthosis Intended to Alter Stiffness Also Alter Orthosis Kinematics," *J of Prosthetics and Orthotics*, **11**, pp. 48–56.
- [25] Lai, J. Y., Kitaoka, H., Kaufman, K., 2001, "Orthosis Stiffness Characteristics," *6th annual GCMAS meeting* Sacramento CA USA April 25–28.
- [26] Klasson, B., Convery, P., and Raschke, S., 1998, "Test apparatus for the measurement of the flexibility of ankle-foot orthoses in planes other than the loaded plane," *Prosthet. Orthot Int.*, **22**(1), pp. 45–53.

- [27] Katdare, K., Schwartz, M., Wervey, R., 2000, "The Non-Linear Stiffness of Ankle Foot Orthoses Measurement and Prediction," *5th GCMAS meeting* Rochester MN USA April 12–15.
- [28] Grood, E. S., and Suntay, W. J., 1983, "A joint coordinate system for the clinical description of three-dimensional motions: application to the knee," *J. Biomech. Eng.*, **105**, pp. 136–144.
- [29] Cole, G. K., Nigg, B. M., Ronsky, J. L., and Yeadon, M. R., 1993, "Application of the joint coordinate system to three-dimensional joint attitude and movement representation: a standard proposal," *J. Biomech. Eng.*, **115**, pp. 344–349.
- [30] Tupling, S. J., and Pierrynowski, M. R., 1987, "Use of Cardan angles to locate rigid bodies in three-dimensional space," *Med. Biol. Eng. Comput.*, **25**, pp. 527–532.

## Description and Validation of a Non-Invasive Technique to Measure the Posture of All Hand Segments

Margarita Vergara

e-mail: vergara@tec.uji.es

Joaquín L. Sancho-Bru

e-mail: sancho@tec.uji.es

Antonio Pérez-González

e-mail: aperez@tec.uji.es

Departamento de Tecnología, Campus de Riu Sec,  
Universitat Jaume I, 12071 Castellón Spain  
Phone 34+ 964 72 81 21 Fax: 34 + 964 72 81 06

*The aim of this work is to describe and validate a technique for measuring the posture of all the segments of the hand in a non-invasive way. The technique uses digital photographic images to reconstruct 3-D location of markers drawn on the skin. The markers are defined to obtain joint rotation angles with physiological meaning. Different experiments have been developed in order to analyze the accuracy and repeatability of the angle measurements. Although the placement of markers does not require any special care, the errors due to their location are lower than 2.6 deg in all cases, thus assuring the repeatability of the technique.*  
[DOI: 10.1115/1.1635403]

## 1 Introduction

Hand-segment movement is usually described in clinical and biomechanical fields by three physiological angles: flexion/extension (F/E), abduction/adduction (Ab/Ad) and pronation/supination (P/S). Distal and proximal interphalangeal (DIP and PIP) joints of fingers and interphalangeal (IP) joint of the thumb are usually considered with 1 degree-of-freedom (DOF) (F/E) [1]. Metacarpophalangeal (MCP) joints are usually considered as 2 DOF joints (F/E and Ab/Ad), as only some passive axial rotation is allowed [2]. The movement of the carpometacarpal (CMC) joint of the thumb is more complex, combining F/E, Ab/Ad and P/S. No movement is usually considered for the second metacarpal (MC2) with respect to MC3 [3], while MC4 and MC5 are considered to have 2 DOF (P/S and F/E) with respect to MC3.

Goniometers, visual techniques or instrumented gloves are used to measure hand postures in clinical, biomechanical and ergonom-

Contributed by the Bioengineering Division for publication in the JOURNAL OF BIOMECHANICAL ENGINEERING. Manuscript received by the Bioengineering Division, November 2, 2003; revision received June 6, 2003. Associate Editor: K. Vaughan.

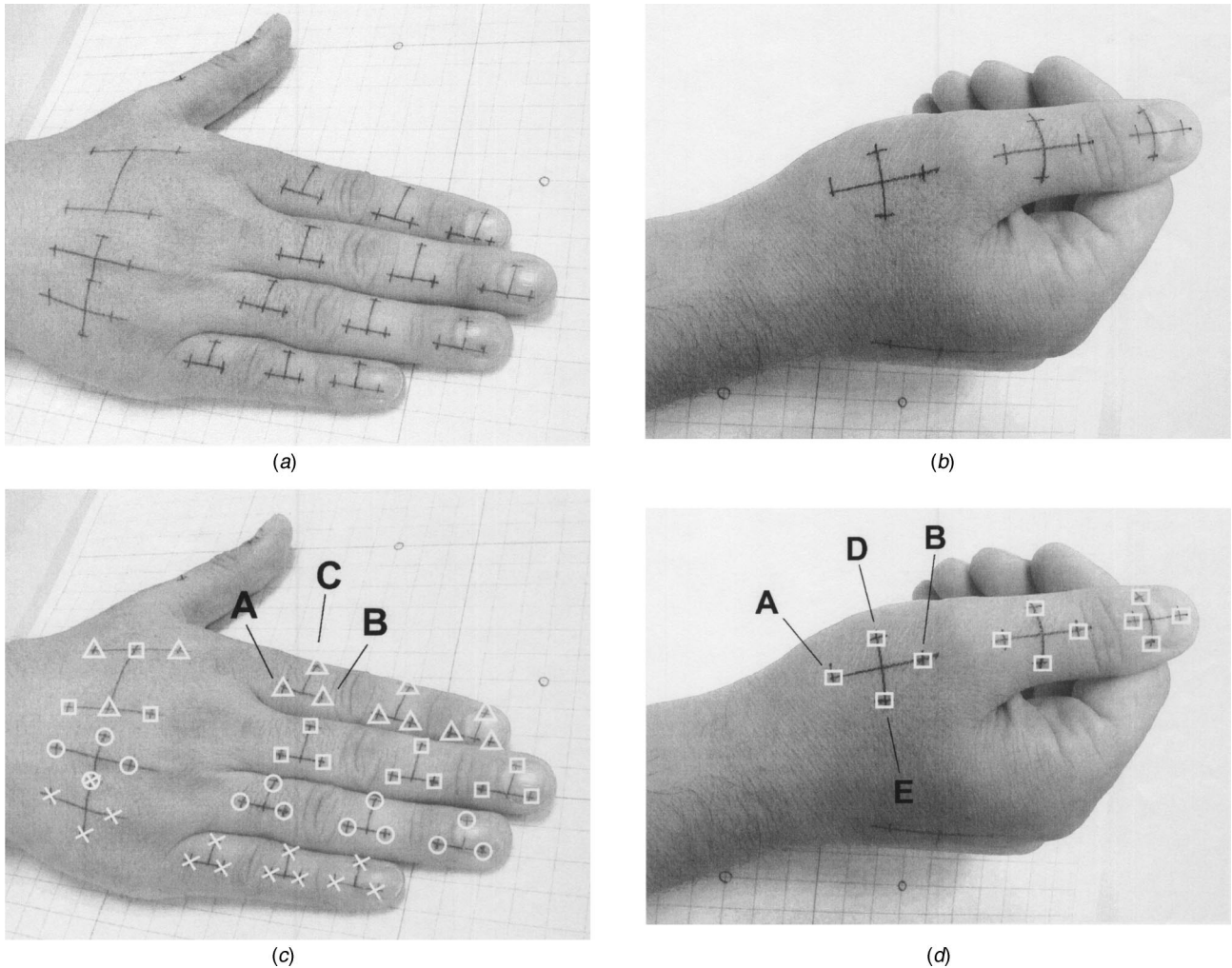


**Fig. 1 Markers and reference postures. (a) Fingers RP with drawn lines and markers; (b) Thumb RP with drawn lines and markers; (c) Markers used for fingers:  $\Delta$  for index finger,  $\square$  for medial finger,  $\circ$  for ring finger and  $\times$  for little finger; (d) Markers used for thumb.**

ics applications [4–7]. Most of these works are limited to the measurement of a few joints and movements (mainly F/E of MCP joints) because of the difficulty of recording the movements of all the small segments of the hand. Three-dimensional measurement for all hand segments is desirable in some applications, as well as expressing the movement in terms of physiological rotation angles. Furthermore, if no instrumentation is allowed for any reason, only visual techniques are suitable. Visual techniques are based on the reconstruction of the coordinates of markers from images [5,8], and have been shown to produce good results for the MCP joint [9]. To the author’s knowledge, no work has been described for measuring the posture of all the segments of the hand simultaneously. The present work presents a technique based on photographs to measure the 3-D relative position of all hand segments in terms of physiological rotation angles without interfering with the natural behavior of the subject as markers drawn on the skin are used.

## 2 Methods

**2.1 Description of the Technique.** The method consists in drawing the markers on segments, taking photos of two reference postures and the one to be measured, reconstructing the 3-D location of markers, and calculating the physiological rotation angles.

**Drawing Markers.** In order to identify the position and orientation of each segment at least three nonaligned markers are needed. The markers should help also the calculation of joint rotation angles, be placed in areas with minimum skin movement and not be hidden. The skin on anatomical landmarks used in other works (generally bone prominences) usually creases or displaces more than in other places and is usually hidden, so that we have selected markers (Fig. 1) drawn on the dorsal face of the segments, separated as much as possible to minimize errors but avoiding joint crease regions. Finger markers are drawn in finger reference posture (RP) and thumb markers in thumb RP (both in Fig. 1). Finger RP corresponds with the resting position of the hand with the palm and fingers laying on a plane surface, keeping the fingers close together. In thumb RP, the tip of the thumb rests on the DIP joint of the index, in a relaxed posture, according to the neutral position of the CMC joint of the thumb presented by Smutz et al. [10].

Index and medial segments present three markers (A, B, and C). Markers A (proximal) and B (distal) are aligned with the bone segment. Markers C are as separated as possible from A and B on the dorsal face. Note that marker C of the index metacarpal is placed on the medial metacarpal and vice versa, assuming no mobility between both segments.

Markers for ring and little fingers differ only in metacarpal markers. They present four markers: A and B again aligned with

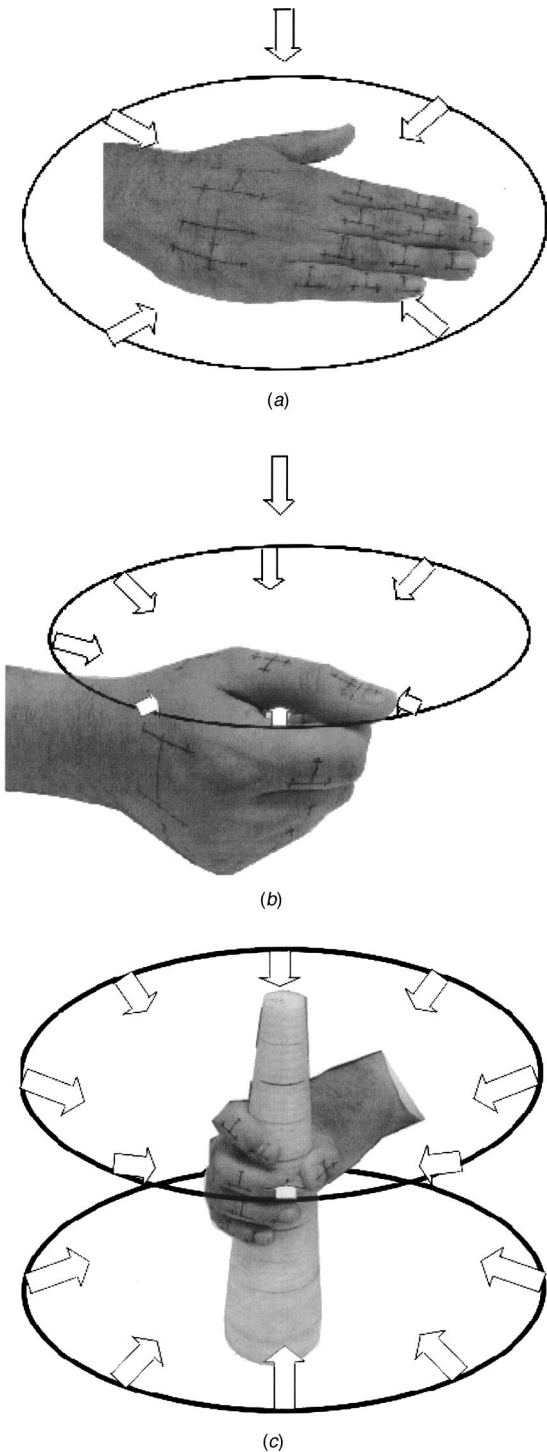


**Fig. 2** Taking photographs for the postures: (a) fingers RP, (b) thumb RP and (c) grasping posture

the segment, and D and E drawn approximately perpendicular to the AB line. In seeking the highest distance between markers, marker D of little metacarpal and marker E of ring metacarpal coincide. This difference is because D and E markers are used to define F/E axis so that D and E markers have to be carefully placed.

Each thumb segment presents four markers (A, B, D, and E markers) also because D and E are used to define F/E axis.

In order to better identify markers on photographs, some lines

are drawn joining them (Figs. 1a and b), but only the points defining markers are important (points with a special symbol in Figs. 1c and d). The inter-marker distance is not important, but the orientation of pairs of markers. The only special care when drawing markers is avoiding the joint crease regions, the alignment of A and B with the segment, and the placement of D and E markers, which define rotation axes orientation.

#### **Taking Photographs and Reconstructing 3-D Coordinates.**

As different markers may be drawn any time, the angles must be referred to a repeatable neutral posture, so that angle measures from different sessions with different markers may be compared. Some previous experiments, not reported in this work, were developed to check the repeatability of different neutral postures similar to those reported by the literature. The most repeatable and easily reproducible have been selected and are those presented above.

To obtain the 3-D coordinates of the markers digital NIKON Coolpix 900 cameras were used to take the photos and PhotoModeler Pro 3.1 software was employed to process them. The calibration of the cameras required for the 3-D reconstruction was performed using the same software.

To minimize errors each marker should appear in at least three photos (minimum is two), with angles between the shots as close to 90 deg as possible. Taking photos with these objectives in mind to track more than 60 markers is a complex task. A standard procedure is followed to facilitate this task. For each RP, from five to eight photos are taken: one shot from the top and the other shots approximately from a ring (Figs. 2a and b). For the grasping posture, more than 14 photographs are taken, distributed approximately in two rings at two heights (Fig. 2c). From all the photos taken, only some of them are selected for each reconstruction: the minimum set that satisfies the above requirements: in practice, it turned out to be three to four photos for each RP, and eight to ten photos for the grasping posture.

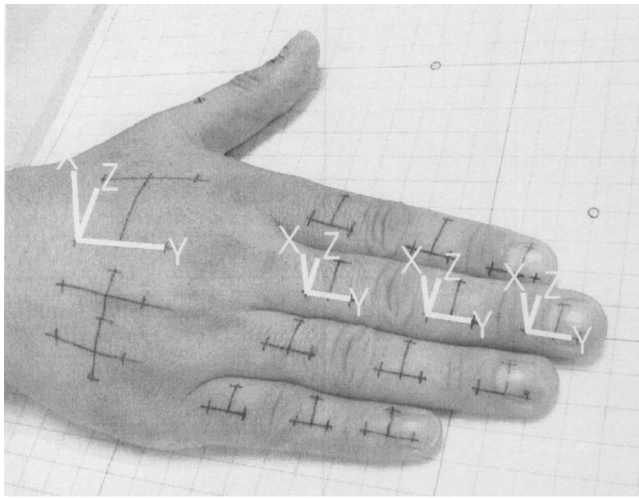
The 3-D location of the markers is obtained on the three sets of photos: the posture analyzed (all markers), finger RP (only fingers markers) and thumb RP (all thumb markers and index metacarpal markers).

**Calculating Angles.** To obtain rotations with physiological meaning, the exact orientation of the anatomical rotation axes should be known. These axes are not strictly perpendicular to the segments, nor between them, as different works have shown [3]. However, in this work perpendicular rotation axes (Cartesian coordinate system) have been assumed.

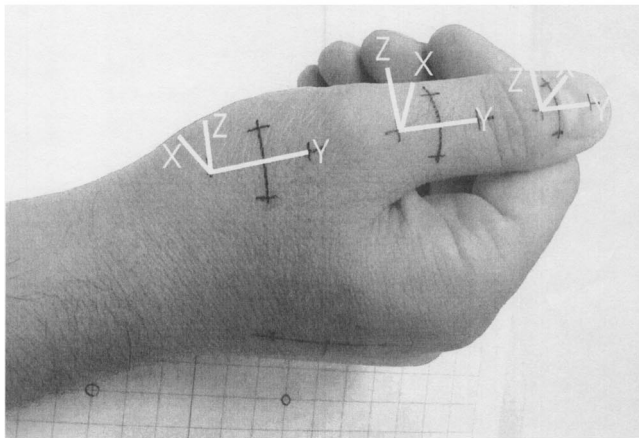
The coordinate systems (CS) are defined in the RPs (Fig. 3) as follows. For all the segments, origin is marker A and Y-axis orientation (P/S axis) is defined with marker B. For segments with three markers (all index and medial segments, and ring and little phalanges), Z-axis orientation (F/E axis) is perpendicular to the Y-axis and parallel to the flat surface on which the hand lies, and finally, X-axis orientation (Ab/Ad axis) is cross product  $Y \times Z$ . For segments with four markers (ring and little metacarpals, and thumb segments) X-axis orientation (Ab/Ad axis) is cross product  $Y \times DE$  line and Z-axis orientation (F/E axis) is cross product  $X \times Y$ .

In the grasping posture, the CSs are defined in the same way, except for the Z-axis orientation in segments with only three markers: it is calculated so that the angle of the plane defined by the three markers with the YZ plane is the same as in the RP.

The rotation angles at each joint are obtained as the Euler rotation angles [11] with sequence Z-X-Y of a CS2 with respect to another CS1 expressed in CS1 according to the description of the rotation axes given by Brand and Hollister [3]. For all joints except CMC ones, CS1 and CS2 are the CSs of the proximal and distal segments at the joint, respectively. For CMC joints, CS1 and CS2 are the CS of the metacarpal segment in the RP and in the grasping posture, respectively.



(a)



(b)

Fig. 3 Coordinate systems for fingers (a) and thumb (b)

## 2.2 Reliability Experiments

Four objectives were followed in the experiments developed: studying the effect of the reconstruction process of marker location on the measured angles (Exp. 1), comparing results of flexion angles with other standard techniques (Exp. 2), checking the repeatability of the RPs (Exp. 3) and studying the repeatability of the whole technique for joint angles measurement (Exp. 4).

Two different tests (Exp. 1) have been used to analyze how joint angles are affected by 3-D coordinate reconstruction errors. In the first test, the same set of photographs from one RP was processed (obtaining 3-D coordinates of the markers) five times and by two operators; the CSs have been defined and the three rotation angles (Z-X-Y) needed to transform proximal to distal CSs at each joint calculated. These angles have been used as the dependent variable in two analyses of variance (ANOVAs) with factors "joint and operator" and "joint," respectively. The first ANOVA was performed to check whether the "operator" factor is significant and the second to calculate the repeatability error as the mean residual standard deviation (MRSD) of the ANOVA. In the second test, nine different sets of photos from the same RP were analyzed; again, the rotation angles were obtained and used in two ANOVAs with factors "joint and photos-set" and "joint" to check the significance of the "photos-set" factor and the repeatability error (MRSD), respectively.

In Experiment 2, index MCP and PIP flexion angles have been measured with an electronic goniometer (G35 of Penny & Giles) and the technique presented in this work, grasping three objects of

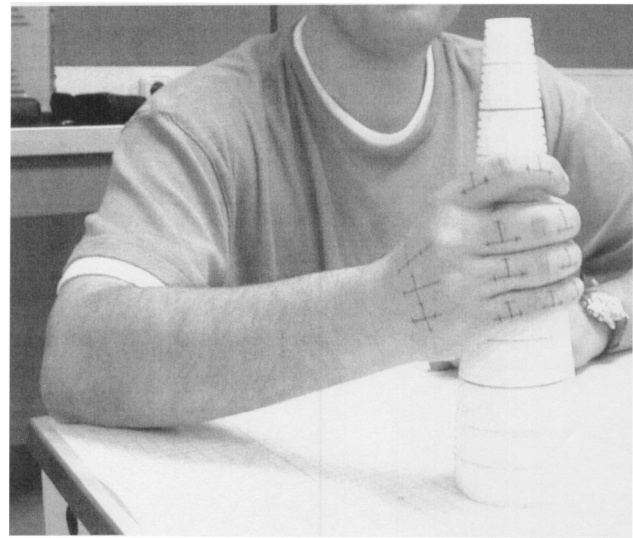


Fig. 4 Grasping posture

different sizes. The bias between the techniques was analyzed using a pair *t*-test of the simultaneous measurements.

In Experiment 3, both RPs were measured on six people. After drawing the markers, the subjects were asked to adopt each RP twice. The repeatability of fingers and thumb RPs was analyzed again in terms of the rotation angles needed to transform the CSs between segments. The global repeatability error was calculated as the MRSD of an ANOVA with factor "subject x joint" for each rotation (F/E, Ab/Ad and P/S). The same analysis was applied to each joint independently and with factor "subject."

In Experiment 4, four people repeated a posture grasping a cone (Fig. 4) several times. Special attention was paid in order to get the same posture for each subject: the elbow resting at the same point with respect to the cone, the fingers at the same height of the cone, etc., although some small differences may exist. After placing the markers and measuring both RPs, the grasping posture was repeated and measured twice. On a different day, with new markers, the test was repeated for all the subjects. The angles of all the segments were obtained for this grasping posture and their repeatability errors estimated from the MRSD of different ANOVAs, with different factors [12]:

- Repeatability error within the same session: factor "subject x joint x day." This variability is only associated with both repetitions of the posture performed in each measurement, i.e. the repeatability error of the posture used.
- Repeatability error in different sessions: considering the mean angles of the two repetitions of each day and the factor "subject x joint." This variability is due only to the repetition of the whole process of marker placement, assuming that the mean grasping posture of each day is the same.

The repeatability errors for each angle of each joint were also calculated from the MRSD of different ANOVAs, within the same session with factor "subject x day," and in different sessions considering the mean angles of the 2 repetitions of each measurement and the factor "subject."

The mean rotation angles of all joints are finally discussed and compared with literature for analyzing the effect of the normal axes considered.

## 3 Results and Discussion

The results of the two tests of Exp. 1 are shown in Table 1. The operator factor and the *photos-set* factor are not significant for any rotation angle. The repeatability errors are lower than 1.3 deg in

**Table 1 Effect of the errors of the 3-D coordinate reconstruction on joint angle calculation. MRSD of the ANOVAs for each angle when photograph processing.**

	With the same set of photos and different processing	With different sets of photos of the same posture
Flexion/extension (deg)	1.007	1.229
Abduction/adduction (deg)	0.483	1.014
Pronation/supination (deg)	1.218	0.188

all cases. This result indicates a high accuracy of angle calculation with photogrammetric reconstruction of coordinates.

The correlation of the flexion angles measured simultaneously with the goniometer and this technique (Exp. 2) is high (correlation coefficient 0.990). No significant differences have been found for them (*t*-test significance level > 0.05, mean and SD of differences are 2.35 deg and 2.76 deg, respectively).

The global repeatability errors for each rotation angle in the RPs, and mean and maximum errors obtained for the analysis of each joint independently (Exp. 3) are shown in Table 2. These

**Table 2 Repeatability of reference postures: Global repeatability errors for each rotation angle in the reference postures (Global MRSD). Mean and maximum MRSD obtained for the analysis of each joint independently.**

	Flexion/extension (deg)	Abduction/adduction (deg)	Pronation/supination (deg)
Global MRSD	1.26	1.35	1.61
Mean MRSD for joints	1.10	1.11	1.43
Maximum MRSD for joints	3.21	2.94	2.36

**Table 3 Repeatability errors for all the joints in the grasping posture.**

	Flexion/extension (deg)	Abduction/adduction (deg)	Pronation/supination (deg)
MRSD within the same session	1.68	1.22	1.54
MRSD in different sessions	2.15	2.08	2.42

results show that the RPs selected are repeatable, as the errors are of a similar magnitude to the photograph processing errors.

Table 3 shows the results of Experiment 4 when considering all the joints and Table 4 with joints considered independently, both within the same session and in different sessions. In general, the errors in different sessions are somewhat larger than in the same session. This difference represents the error associated to the new placement of the markers and the error associated to the repeatability of the RPs, and is not bigger than 2.6 deg in any case. Considering the error associated to the repeatability of the RPs obtained previously (Table 2), the repeatability error associated to the markers is quite small.

Mean angles for the grasping posture are shown in Table 5. IP joint of the thumb is flexed, and MCP and CMC joints slightly extended and abducted with respect to the neutral posture, with some pronation. The fingers are flexed over the cone. MCP joints have a similar flexion angle for all fingers, being slightly abducted from the RP. Except for the index finger, flexion is accompanied by supination (greater towards little finger), which indicates that the flexion rotation axes are not perpendicular to the segments. This result was expected from the different shape of the metacarpal heads of each finger, which facilitates the finger's converging towards a same point [13]. Unless real physiological rotation axes, instead of perpendicular axes, are used, this effect will always be present. Flexion at PIP joints decreases from index to little finger in order to adapt the hand to the shape of the cone. Again, as F/E rotation axis is not perpendicular to the segment, except for the medial finger, flexion is accompanied by abduction as well as by pronation in medial and index fingers, and supination in ring and little fingers, facilitating the above-mentioned finger converging. A similar behavior is observed for DIP joints, with smaller flexion angles.

**Table 4 MRSD of the rotation angles obtained for the grasping posture in the same session and in different sessions with joints considered independently. 1. thumb, 2. index, 3. medial, 4. ring, 5. little.**

	Flexion/extension (deg)		Abduction/adduction (deg)		Pronation/supination (deg)	
	Same session	Different session	Same session	Different session	Same session	Different session
CMC1	1.03	2.92	0.99	1.85	2.40	1.03
MCP1	1.26	2.02	1.38	0.33	1.92	3.75
IP1	2.30	2.77	1.20	1.63	1.26	1.28
MCP2	1.28	2.34	1.92	1.84	2.04	1.34
PIP2	0.57	0.76	1.12	1.68	0.92	1.84
DIP2	1.43	1.33	0.42	2.14	0.80	2.71
MCP3	2.01	1.55	1.22	1.74	1.40	2.40
PIP3	1.65	0.83	1.58	1.70	1.35	2.00
DIP3	2.37	3.42	0.88	1.21	0.99	1.98
CMC4	0.82	1.73	0.47	1.94	1.35	2.39
MCP4	1.75	1.99	1.27	1.35	1.81	4.16
PIP4	1.33	1.79	0.81	3.05	1.63	2.18
DIP4	1.21	0.62	0.86	3.42	1.19	1.85
CMC5	1.27	1.30	0.31	2.11	1.82	0.51
MCP5	2.30	2.95	1.83	2.35	1.44	3.12
PIP5	1.69	2.36	1.87	1.31	1.48	3.13
DIP5	2.40	2.79	1.04	3.25	1.32	2.10
<b>Mean MRSD</b>	<b>1.57</b>	<b>1.97</b>	<b>1.13</b>	<b>1.94</b>	<b>1.48</b>	<b>2.22</b>

**Table 5 Mean rotation angles for each joint in the grasping posture. Positive values for flexion and supination of all joints, for abduction of index, medial and thumb joints, and for adduction of ring and little joints. 1. thumb, 2. index, 3. medial, 4. ring, 5. little.**

Joint	Flexion/extension (deg)	Abduction/adduction (deg)	Pronation/supination (deg)
CMC1	-12.46	12.30	-12.34
MCP1	-4.38	16.41	-18.92
IP1	36.32	3.07	-0.32
MCP2	44.89	-0.26	3.91
PIP2	58.79	10.62	-3.33
DIP2	39.84	7.55	-5.26
MCP3	57.30	5.97	24.69
PIP3	57.76	0.41	-3.01
DIP3	38.49	5.92	-7.06
CMC4	5.48	-4.55	0.44
MCP4	52.74	-8.52	29.64
PIP4	52.33	-13.08	11.42
DIP4	30.79	-10.52	-1.70
CMC5	6.32	-5.94	2.13
MCP5	53.21	-11.23	30.06
PIP5	29.47	-8.86	6.24
DIP5	25.39	-2.14	-3.11

Because of the use of perpendicular rotation axes, rotations about the three axes are obtained in joints where 1 or 2 physiological DOEs were expected. Although we have talked about F/E, Ab/Ad and P/S rotations, they should be considered only as rotation about the Z, X and Y axes defined, because they are not exactly the same as the physiological ones. Nevertheless, the validity of this technique is based on its repeatability (less than 2.6 deg of error due to the marker placement in any joint), even when the markers are located without specific anatomical knowledge or special care.

#### 4 Conclusions

The technique developed is based on the reconstruction of 3-D coordinates of points marked on the skin from photographs. The location of these markers does not need specific anatomical knowledge or special care. Markers coordinates in both the posture to be measured and in two reference postures are obtained, and from them, joint rotation angles about three perpendicular axes. Hand posture is expressed with joint rotation angular terminology commonly used in biomechanical fields, although in some cases these axes do not correspond exactly with the physiological ones.

The reliability experiments performed show that the measurement process is reliable and accurate enough, and no significant difference is found with goniometer flexion measurements. The technique is repeatable and very little affected by possible differences in the marker placement, with a maximum error due to marker placement lower than 2.6 deg.

The technique allows hand posture measurement in a non-invasive way and is more complete than other techniques (it measures all movements of all segments). With some improvements, it may be used to observe 3-D movement ranges of the hand segment for clinical applications and to measure the hand posture of subjects during real tasks for ergonomics purposes, as well as dynamic actions, if digital video images and automated recognition of markers are used.

#### Acknowledgments

We thank the support of the *Fundació Bancaixa* and the *Universitat Jaume I* for the project Ref. P1A97-06, in which this work is partially included.

#### References

- [1] Dubousset, J. M. 1981, *The Digital Joints*. (In: Tubiana, R., ed. 'The hand. Volume 1'.) Philadelphia: Saunders Company, pp. 191–201.

- [2] Kapandji, I. A. 1997, *Physiologie Articulare, 1: Membre Supérieur*. Paris: Maloine.
- [3] Brand P. W., and Hollister, A. M., 1992, *Clinical Mechanics of the Hand*. Second Edition. St. Louis: Mosby-Year Book, Inc.
- [4] Lee, J. W., and Rim, K., 1991, "Measurement of finger joint angles and maximum finger forces during cylinder grip activity." *J. Biomech. Eng.*, **13**, 152–162.
- [5] Rash, G. S., Belliappa, P. P., Wachowiak, M. P., Somia, N. N., and Gupta, A., 1999, "A demonstration of the validity of a 3-D video motion analysis method for measuring finger flexion and extension." *J. Biomech.*, **32**, 1337–1341.
- [6] Yun, M. H., and Freivalds, A., 1998, *Analysis of tool grip tasks using a 3D glove*. (In: Kumar, S. ed. 'Advances in Occupational Ergonomics and Safety 2'.) Amsterdam: IOS Press, 401–404.
- [7] Hsiao, H., Keysersling, W. M., 1990, "A three-dimensional ultrasonic system for posture measurement." *Ergonomics*, **33**(9), 1089–1114.
- [8] Small, C. F., Pichora, D. R., Bryant, J. T., and Griffiths, P. M., 1993, "Precision and accuracy of bone landmarks in characterizing hand and wrist position." *J. Biomech. Eng.*, **15**(5), 371–378.
- [9] Speirs, A. D., Small, C. F., Bryant, J. T., Pichora, D. R., and Zee, B. Y., 2001, "Three-dimensional metacarpophalangeal joint kinematics using two markers on the phalanx." *Proc. Inst. Mech. Eng.*, **215**(4), 415–419.
- [10] Smutz, W. P., Kongsayreepong, A., Hughes, R. E., Niebur, G., Cooney, W. P., and An, K. N. 1998, "Mechanical advantage of the thumb muscles." *J. Biomech.*, **31**, 565–570.
- [11] Small, C. F., Bryant, J. T., and Pichora, D. R., 1992, "Rationalization of kinematic descriptors for three-dimensional hand and finger motion." *J. Biomech. Eng.*, **14**(2), 133–141.
- [12] Altman, D. G., and Bland, J. M., 1983, "Measurement in medicine: the analysis of method comparison studies." *The Statistician*, **32**, 307–317.
- [13] Craig, S. M., 1992, "Anatomy of the joints of the fingers." *Hand Clin.*, **8**(4), 693–700.

## The Influence of Inflow Boundary Conditions on Intra Left Ventricle Flow Predictions

Q. Long,\* R. Merrifield, and G. Z. Yang

Faculty of Engineering, Imperial College London, South<sup>1</sup> Kensington Campus, London SW7 2AZ, UK

P. J. Kilner and D. N. Firmin

Cardiovascular MR Unit, Royal Brompton Hospital, Imperial College London, SW3 6NP, UK

X. Y. Xu<sup>1</sup>

*The combination of computational fluid dynamics (CFD) and magnetic resonance imaging (MRI) offers a promising tool that enables the prediction of blood flow patterns in subject-specific cardiovascular models. The influence of the model geometry on the accuracy of the simulation is well recognized. This paper addresses the impact of different boundary conditions on subject-specific simulations of left ventricular (LV) flow. A novel hybrid method for prescribing effective inflow boundary conditions in the mitral valve plane has been developed. The detailed quantitative results highlight the strengths as well as the potential pitfalls of the approach. [DOI: 10.1115/1.1635404]*

#### 1 Introduction

Techniques based on Computational Fluid Dynamics (CFD) have been used to investigate Left Ventricular (LV) flow for many years and have recently undergone substantial improvements [1–9]. In most existing ventricular flow simulations, the aortic and mitral valves are not modeled explicitly. Instead, they are typi-

\*Corresponding author: Brunel Institute for Bioengineering and Dept of Mech. Eng., Brunel University, Uxbridge, Middlesex, UB8 3PH, UK. e-mail: quan.long@brunel.ac.uk.

Contributed by the Bioengineering Division for publication in the JOURNAL OF BIOMECHANICAL ENGINEERING. Manuscript received December 12, 2002 by the Bioengineering Division; revision received June 20, 2003. Associate Editor: J. Moore.

cally simplified as an inflow or outflow boundary that opens and closes at specified times. One key issue here is that when the mitral valve is open during diastole, appropriate inflow conditions at the valve plane must be specified.

There are two different methods that are commonly used to specify the boundary conditions at model boundaries in CFD. The first is based on the use of Dirichlet boundary conditions that specify the values of the variables used. The second utilizes Neumann boundary conditions that specify the gradient of these variables rather than their actual values. For both of these approaches, it is essential that global mass conservation is satisfied throughout the simulation. This implies that the mass flow rate at the inflow boundary should match, within machine accuracy, the mass drawn into the LV due to change in ventricular volume. In practice, this is difficult to achieve in cases where either the velocities (Dirichlet condition) or the mass flow rates (Neumann condition) at the inlet are specified due to the difficulty of calculating the LV volume change to machine accuracy. Pressure boundary conditions, a type of Neumann conditions where constant normal velocity gradient as well as pressure values were imposed, allow global mass conservation to be controlled automatically by the CFD code itself. However, Neumann conditions assume that the flow is fully developed with a constant cross-sectional area. Unfortunately, the mitral valve is located immediately above a region that undergoes sudden expansion. The error introduced by the assumption is likely to be significant.

The purpose of this paper is to explore a new method of prescribing boundary conditions based on a hybrid approach. This combines the specification of velocities for the majority of the inlet area to define velocity profile at boundary plane and the specification of pressure for the remainder inlet to satisfy global mass conservation. Comparisons were made with simulations performed using the proposed method as well as pure pressure boundary conditions. Issues related to the optimal location and relative areas of the velocity and pressure patches were also investigated. Flow simulations were performed by using prescribed LV wall movement, which was obtained by MR from a healthy volunteer.

## 2 Methods

A volunteer with no history of heart disease was chosen for this study. The study comprised the following steps: (1) magnetic resonance imaging (MRI) of the LV, (2) the construction of a dynamic model from the resulting images, and finally, (3) the generation of a volumetric mesh, its temporal interpolation and the subsequent CFD simulation.

**2.1 MR Data Acquisition and Image Processing.** Imaging was performed using a Siemens Sonata 1.5T MR system. A True-FISP cine sequence was used to acquire 14 short axis slices each with 16 phases providing complete spatial and about 80% temporal coverage of the cardiac cycle (all systolic and part diastolic phases) with a temporal resolution of 48 ms. Each slice was acquired in a single 20-second breath-hold so as to minimize artefacts introduced by respiratory movement. Segmentation and reconstruction of the LV structure were performed using proprietary software. This allowed detailed spatial and temporal properties of the endocardial border to be captured from reformatted images representing short axis, long axis and M-Mode acquisitions.

**2.2 Structured Mesh Generation and CFD Simulation.** For each time phase, the LV cavity was subdivided into 24 blocks within which structured grids of hexahedral cells were generated. Details of the mesh generation scheme can be found in [10]. The final model contained 54,230 nodes and 41,000 cells. Cubic spline interpolations were performed to obtain a total of 49 time-dependent meshes in the cardiac cycle from the 16 meshes generated from the original LV MR data.

The Navier-Stokes equations for 3-D unsteady laminar flow with moving walls were solved using a finite-volume based CFD

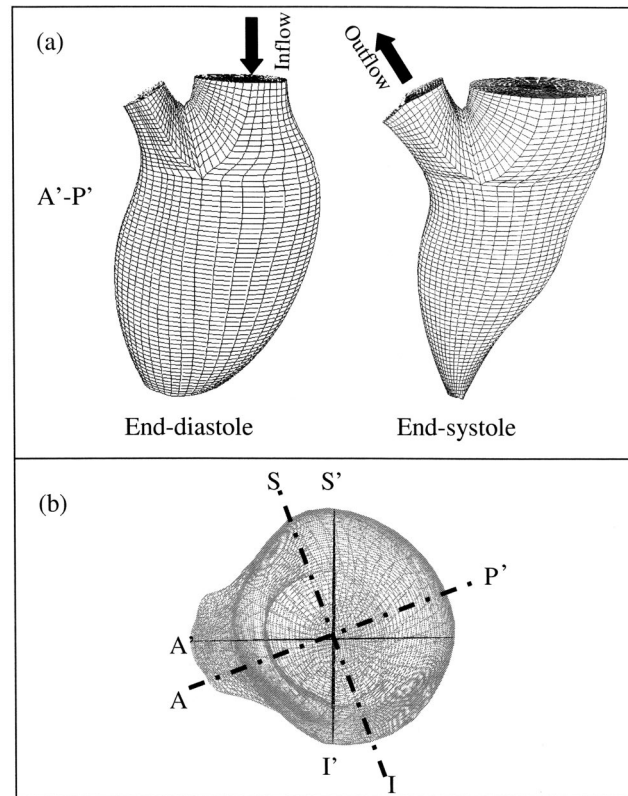


**Fig. 1** Illustration of model surface meshes (a), and the definition of chosen plane locations (b). The chosen plane A'-P' is approximately anterior-posteriorly orientated, aligned with both the inflow and outflow tracts. Plane I'-S' is approximately inferior-superiorly orientated and is orthogonal to the A'-P' plane.

solver—CFX4 (AEA technology). The blood was treated as an incompressible Newtonian fluid with a constant viscosity of 0.004 Pa s. The simulation was started from the beginning of systole with the pressure of the aortic valve plane set to zero and with the mitral valve plane treated as a non-slip wall. At the onset of diastole, the aortic valve was closed by treating it as a wall, whilst the mitral valve was opened by using a combination of pressure and flow boundaries. The simulation was repeated for four cycles in order to reach a periodic solution. The results that were obtained in the fourth cycle are presented.

To understand the influence of the imposed inflow boundary conditions on predicted flow patterns, four sets of numerical experiments were designed. Firstly, the effect of varying the inflow opening area of a boundary with an imposed pressure boundary condition was investigated. To do this, three simulations ( $P_a$  to  $P_c$ ) were performed each utilizing a different opening area. The pressure at the center of each cell face at the inlet was set to zero.

The second experiment was designed to test the effect of varying the inflow area when using hybrid boundary conditions. three simulations ( $V_a$  to  $V_c$ ) were performed with the same inflow area ratios used in the first experiment. This time, however, the inflow area  $A_{in}$  was divided into two regions including a pressure boundary area  $A_p$  and a velocity boundary region  $A_v$ . In this study, the velocity boundaries were specified to have a uniform velocity profile. The mean velocity at a given time  $t$  was derived from the change in volume between successive time steps. The flow was assumed to be perpendicular to the valve plane. Zero pressure was defined at the pressure boundary patch.

Finally, for cases where the hybrid boundary condition was used, the influence of the location and size of the pressure boundary patch on the predicted flow patterns was investigated. The

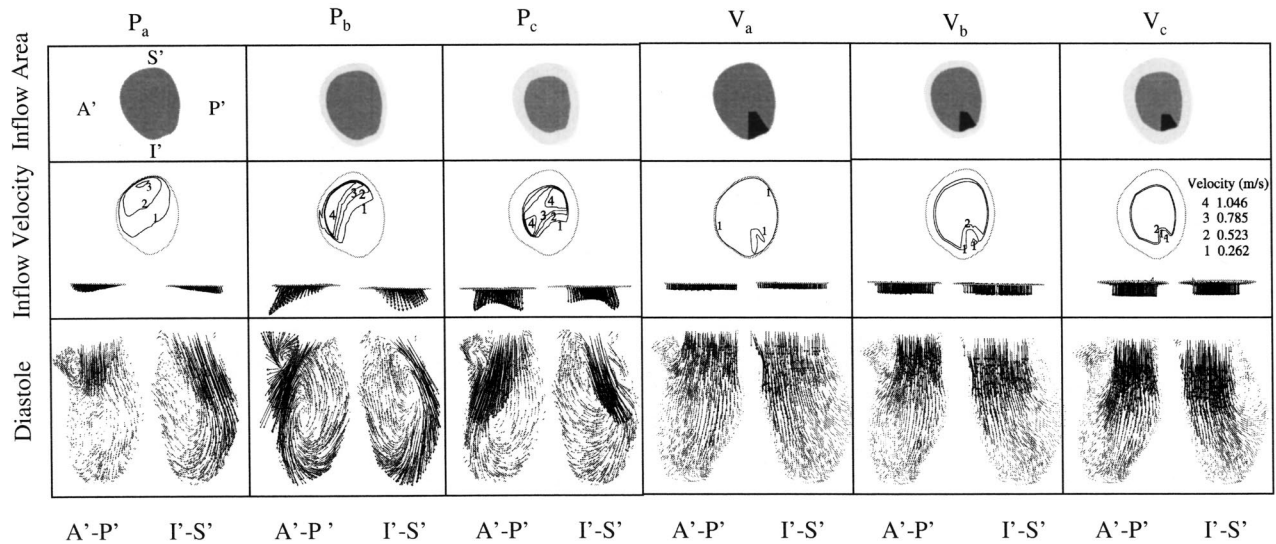


**Fig. 2 Simulation results with pressure boundary condition (columns 1 to 3) and hybrid boundary conditions (columns 4 to 6) prescribed at the inflow plane. First row defines the inflow area and pressure patch location. Second row presents the derived velocity contours (upper panel) and profiles (lower panel) at the inflow plane at the mid-diastole ( $t/t_p=0.78$ ). Third row presents velocity vectors viewed from A'-P' and I'-S' directions at the same time.**

third and fourth experiments involved simulation using six different pressure patch locations (cases  $L_a$  to  $L_f$ ) and six different sizes (cases  $A_a$  to  $A_f$ ) respectively.

### 3 Results

#### 3.1 Geometrical Reconstruction and Mesh Generation.

Figure 1(a) shows the 3-D surface mesh of the LV at end-diastole and end-systole at approximate Anterior-Posterior view. It is evident that significant variations in shape and volume occur over the cardiac cycle. In addition to this, the area of the inflow tract  $A_{total}$  also changes considerably. Due to the lack of sufficiently detailed anatomical information from the MR images, the leaflets of the mitral and aortic valves were not modeled. Likewise, the exact location of the valve ring could not be derived. Instead, the boundary planes were placed roughly 5 mm above the ventricular base, just within the left atrium and the ascending aorta. Predicted velocities are presented in two orthogonal planes along the long axis of the ventricle. The commonly used orientations in medical imaging are shown in dashed lines in Fig. 1(b) as a reference. Throughout this paper, cross sections A'-P' and I'-S' are used for presenting the derived velocity vectors as they provide a better depiction of flow through the inflow and outflow tracts.

#### 3.2 Flow Predictions With Pressure and Hybrid Inflow Boundary Conditions.

Figure 2 shows the CFD predictions for cases  $P_a$  to  $P_c$  and  $V_a$  to  $V_c$ , respectively. The first row defines the inflow area ( $A_{in}$ ), pressure patch size and location (for  $V_a$  to  $V_c$ ) used in each case. The area ratios of  $A_{in}/A_{total}$  were 100% ( $P_a$  and  $V_a$ ), 70% ( $P_b$  and  $V_b$ ), and 50% ( $P_c$  and  $V_c$ ) respectively. The derived velocity profiles at the inflow plane during mid-diastole ( $t/t_p=0.78$ ) are presented in the second row with velocity contours and the corresponding velocity profiles at two different viewing angles. It was found that the resultant velocity were generally skewed towards the A'-S' direction in cases  $P_a$  and  $P_b$ . Two high velocity regions were found in case  $P_c$ , indicating the profile was about to switch directions. At mid-diastole ( $t/t_p=0.78$ ), a strong inflow jet was clearly evident in all three pressure boundary cases in predicted velocity vectors in the third row of Fig. 2. However, directions of the jet varied significantly depending on the area  $A_{in}$ . In case  $P_a$ , the jet was slightly skewed towards the superior wall. The jet skewed strongly towards the anterior and superior walls in cases  $P_b$  and  $P_c$ , with anti-clockwise

and clockwise vortices in the A'-P' and I'-S' planes, respectively. With the exception of the A'-P' plane in case  $P_a$ , the flow patterns remained similar towards the end of diastole because of the strong swirling inside the ventricular cavity. Consistent inflow profiles were observed throughout diastole for all cases.

In the first row (columns 4 to 5) of Fig. 2, a dark region is shown in the inflow area ( $A_p$ ) in each of the three cases with hybrid boundary conditions ( $V_a$  to  $V_c$ ) to represent the pressure patch defined. 'Plug' flow profiles can be found in all three cases with lower velocities in the pressure patch region. In the third row, a significantly more uniform inflow jet directed towards the apex was observed in each case with a varied jet velocity. During mid-diastole ( $t/t_p=0.78$ ), a clockwise vortex can be seen in the A'-P' plane for all cases. The main vortex center was located at the left side of the jet. The dominant vortex in the I'-S' plane was anti-clockwise.

The obvious differences in flow patterns between the cases with pressure and hybrid boundary conditions have been demonstrated. It is evident that the inflow velocity profile is the main factor that causes the differences. As described above, the inflow velocity profiles for pure pressure boundary cases were generated by the simulation itself with imposed constant normal velocity gradients at each computational cell at the boundary patch. The profiles achieved in this manner could be significantly different from the true profiles. With the hybrid approach, the resultant inflow profiles were very close to the prescribed velocity because the profiles were imposed directly on the main region of the boundary.

#### 3.3 Sensitivity Analysis on Hybrid Boundary Conditions.

As mentioned earlier, the purpose of defining a small pressure boundary patch at the inflow boundary is to help to achieve global mass conservation during the CFD calculation. However, the velocity profile inside the pressure patch cannot be controlled and this may result in different inflow profiles from the prescribed one. The size of the pressure patch  $A_p$  has to be chosen carefully so that it is not too large of causing a noticeable difference between the resulted and prescribed inflow profiles. On the other hand, it should not be too small to be sensitive to the prescribed velocity value of  $V_0(t)$ .

Figure 3 shows the velocity profile obtained with a pressure patch located at different locations of the inflow area  $A_{in}$  on a model with  $A_{in}/A_{total}=70\%$ . Six different locations were tested,

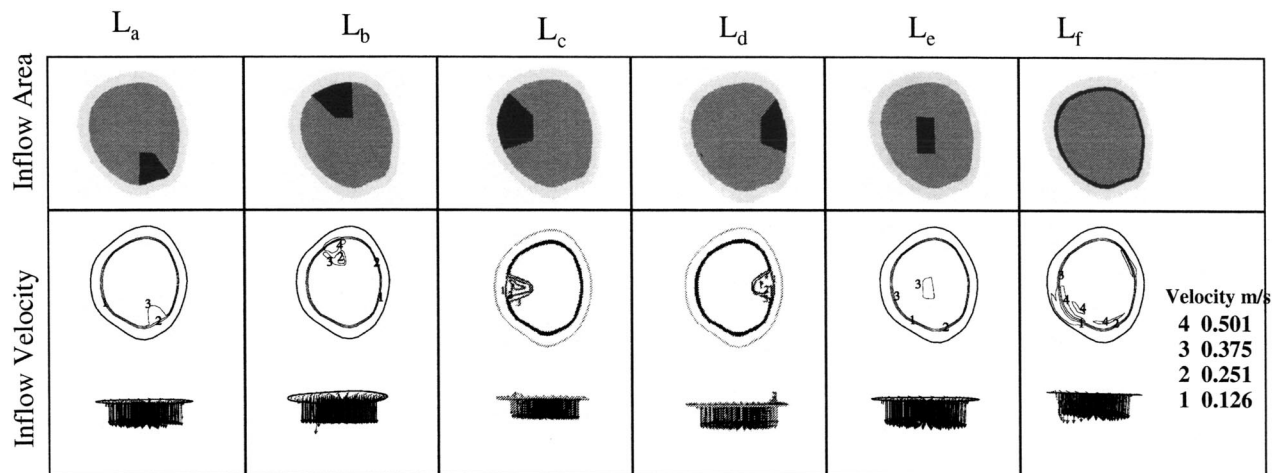


**Fig. 3** Simulation results with hybrid boundary conditions at the inflow plane with different pressure patch locations. First row defines the pressure patch location and second row presents resulted velocity contours (upper panel) and profiles (lower panel) at the mid-diastole ( $t/t_p=0.78$ ).

as shown in the first row of Fig. 3. Cases  $L_a$  to  $L_d$  had pressure patches attached to part of the boundary wall, whereas for cases  $L_e$  and  $L_f$  the pressure patch was in the center and the outer ring of  $A_{in}$ , respectively. For the six cases presented, the cycle average ratios of  $A_p/A_{in}$  were: 9.29%, 11.37%, 9.14%, 9.06%, 8.41%, and 14.4% respectively. “Plug” flow profiles can be seen in all cases but with small velocity variations in the pressure patch region on the resulting velocity profiles at inflow plane in the second row of Fig. 3. The mean velocity value was  $V_0(t)=0.417$  m/s at this time phase. In cases  $L_a$  and  $L_e$ , there was a sudden dip in velocity in the pressure patch region. A more gradual change in velocity can be found in case  $L_b$  with low velocities (contour value 2) near the center and high values close to the wall (contour value 4) in the pressure patch. Low velocities were found at the center of the pressure patch for cases  $L_c$  and  $L_d$  with a small amount of flow reversal. More complex patterns were observed in case  $L_f$  where there were a few isolated high velocity spots around the wall. These regions were small, however, and the maximum velocity

was about 20% higher than  $V_0(t)$ . Although no velocity patterns were presented in Fig. 3 due to space limitation, overall flow patterns were very similar among the six cases.

To investigate the effect of varying the area ratio between the pressure patch and the inflow boundary plane area, CFD simulations were performed for six different pressure patch sizes. The area ratio of  $A_{in}/A_{total}$  remained 70% but with  $A_p/A_{in}$  being 4.56%, 8.4%, 14.02%, 20.23%, 28.65% and 28.35% for cases  $A_a$  to  $A_f$  respectively. The locations of the pressure patch are shown in the first row of Figure 4, which are mostly located on the I'-P' side with the exception of case  $A_f$ .

The resulting velocity profiles at the inflow boundary for the six cases are shown in the second row of Fig. 4. From the vector plot, high velocities appeared in cases  $A_d$ ,  $A_e$  and  $A_f$ . The worst case was  $A_f$  which demonstrated a maximum velocity of almost three times the value of  $V_0(t)$ . A similar situation can be found in  $A_e$ . For  $A_d$  the maximum velocity was about 40% higher than  $V_0(t)$ .

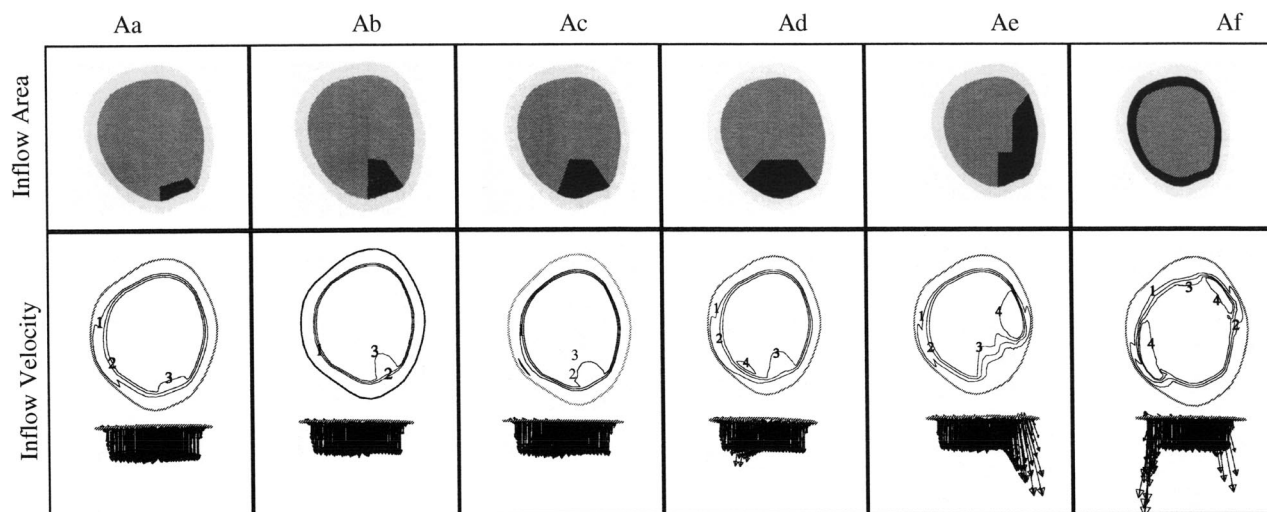


**Fig. 4** Simulation results with the hybrid boundary condition at the inflow plane with different pressure patch sizes. The figure format, velocity scales as well as the chosen time phase were the same as those in Fig. 3.

The velocity profiles and contours appeared fairly flat in cases  $A_a$ ,  $A_b$  and  $A_c$ . Velocity vectors in LV were almost identical in cases  $A_a$  to  $A_c$ .

## 4 Discussions

Using in vivo MR measured ventricular morphology and wall movement, it is possible to perform subject specific flow simulations. In the absence of an explicit representation of the mitral valve in the computation model, the inflow boundary conditions imposed at the mitral valve plane play a crucial role in determining the detailed flow structure inside the LV. This study shows that the predicted flow patterns can vary significantly if different boundary conditions are imposed.

As described in the introduction, the assumption of fully developed flow when a pressure boundary condition is imposed would be inappropriate if the inflow boundary was close to a region that experienced sudden contraction or expansion. To assess the uncertainties introduced by this assumption, a series of numerical models were generated with various degrees of expansion (different area ratios of  $A_{in}/A_{total}$ ) with pressure boundary condition imposed. Calculated inflow velocity profiles showed surprising degrees of skewing. Inflow profiles and LV flow patterns showed excessive variability as  $A_{in}$  was changed. Pure pressure boundary conditions should therefore be avoided for LV flow simulation if the inflow orifice area ( $A_{in}$ ) cannot be accurately defined.

In CFD models, to avoid the problems introduced by a sudden change of area within an inflow region, a tube may be attached to the inlet. By defining an inflow region with a constant area at the far end of this tube, the boundary can be moved away from the highly dynamic region. However, this scheme is not appropriate for ventricular simulations. The direction and shape of the inflow and outflow tracts of the left ventricle typically change dramatically during the cardiac cycle. If the tube is to be a natural extension of the inflow tract, the whole tube must move significantly. This movement would cause the fluid particles inside the tube to oscillate and would therefore generate highly complex flow patterns.

Having realized the importance of the inflow velocity profile, researchers have attempted to define velocities on the inflow region accurately. Despite the difficulty in achieving global mass conservation, Dirichlet velocity boundary conditions were defined for the inlet in recently reported 2-D studies [2,5] that used (solid/fluid) coupled modeling. In Chahboune's work, a 'plug' profile was defined on the inflow boundary. The LV volume change was obtained by integrating the model boundary movement in a 2D model. However, no further discussion was made concerning the possible mass imbalance of the fluid simulation. In Vierendeels' work, a measured transmitral velocity profile was defined on the inflow boundary. To achieve the global mass conservation, an artificial compressibility method was employed. For example, if a larger volume of fluid is entering the LV than the volume displaced by the boundary, pressure will rise in cells with a mass imbalance, leading to a corresponding rise in pressure at the cardiac wall. The pressure rise at the wall is then used as an input for the heart wall model, leading to a displacement of the cardiac wall. However, the procedure may be difficult to converge in 3-D geometry. The idea of defining an artificial wall movement from imbalanced mass is also difficult to apply to a pure CFD simulation with prescribed LV wall motion.

In the simulations that used hybrid boundary conditions, the careful selection of the location and size of the pressure patch allowed the inflow velocity profiles to be well controlled. Consequently, the predicted flow patterns only varied gradually with changes in the area  $A_{in}$ . Although no direct comparison was made between the predicted flow patterns and MR measurements in this study, the main flow features obtained from cases  $V_a$  to  $V_d$  were similar to those reported in the literature [11].

It must be noted that the use of hybrid boundary conditions does not come without risks. The inflow profile can be very dif-

ferent from the prescribed one if the pressure boundary patch is inappropriately defined. The location and size of the pressure patch affected the inflow profiles to different extents. Results for cases  $L_c$  and  $L_d$  indicate that a pressure patch located at the  $A'$  or  $P'$  wall would produce more disturbed velocity profiles than those in case  $L_a$ . It is natural to assume that a pressure patch on the boundary of the inflow plane, such as case  $L_f$ , might not influence the overall flow patterns to a great extent. However, high velocity could occur at isolated locations as shown in Figure 4 ( $L_f$ ), thereby influencing the overall flow patterns. In contrast, pressure patches located along the  $I'-P'$  walls (case  $L_a$ ) performed significantly better. The pressure patch located in the center of the plane produced reasonably uniform profiles as shown in the contour plot. However, the influence on flow predictions is still noticeable. The optimal location of the pressure patch for the subject studied was adjacent to the  $I'-P'$  wall. The hybrid boundary condition has by now been applied to seven normal subject LV flow simulations. The preliminary results showed that pressure patch located adjacent to the  $I'-P'$  wall normally produced better results.

The influence of the size of the pressure patch on the resulting inflow profiles can be understood more easily. For a fixed mass flow rate, the profile inside the pressure patch can take different shapes with low velocities at one side and high velocities at the other. This variability is exasperated by an increase in the pressure patch size (such as in cases  $A_d$  and  $A_c$ ). The results show that for the pressure patch located at the  $I'-P'$  side with an area ratio of  $A_p/A_{in}$  smaller than 15%, the resulting inflow profiles are similar to the prescribed ones and the variation of velocity inside the pressure patch can be ignored.

It should be pointed out that the results presented here are based on the assumption of a 'plug' inflow which approximates reported measurements [12,13]. The mitral valve plane orientation was fixed in the study; therefore the direction of the inflow jet did not change with time. In vivo MR measurements have shown that the orientation and the location of the mitral valve plane as well as the direction of the inflow jet are time dependent. The influence of the mitral annular motion to LV flow predictions will be investigated in future studies. It also needs to be noted that no quantitative validation of the CFD predictions with in vivo data has been made here since the present study is focused on improving the stability and reliability of CFD simulation.

## 5 Conclusions

The CFD simulation of left ventricular flow is highly sensitive to the boundary conditions imposed during diastolic filling. In this study, the prescription of Neumann pressure boundaries produced inflow velocity profiles with surprising degrees of skewing. Inflow profiles and intra-cavity flow patterns showed excessive variability as the area of the inflow orifice was changed. Computed inflow profiles were found to conform more closely to expected inflow profiles when hybrid conditions were applied to the boundary. The location and size of the pressure region in hybrid boundary condition influenced resultant profiles and flow patterns. An ideal pressure patch design should ensure that velocity profiles near the inflow plane are continuous and smooth. Generally, pressure patch located adjacent to the  $I'-P'$  wall tends to produce better results. For the subject studied, a pressure region located inferior-posteriorly, with an area of less than 15% of the total inflow area, resulted in velocity profiles and flow patterns that most closely resemble in vivo measurements.

## Acknowledgments

This work was sponsored by the British Heart Foundation (FS/2001002). The authors would like to thank Drs Peter Gatehouse and Jenny Keegan for their assistance with the acquisition of the MR data.

## References

- [1] Peskin, C. S., and McQueen, D. M., 1980, "Modelling prosthetic heart valves for numerical analysis of blood flow in the heart," *J. Comput. Phys.*, **37**, pp. 113–32.
- [2] Chahboune, B., and Crolet, J. M., 1998, "Numerical simulation of the blood-wall interaction in the human left ventricle," *Eur. Phys. J.: Appl. Phys.*, **2**, pp. 291–97.
- [3] Peskin, C. S., and McQueen, D. M., 1992, "Cardiac fluid-dynamics," *Crit. Rev. Biomed. Eng.*, **20**, pp. 451–59.
- [4] Lemmon, J. D., and Yoganathan, A. P., 2000, "Computational modelling of left heart diastolic function: examination of ventricular dysfunction," *ASME J. Biomech. Eng.*, **122**, pp. 297–303.
- [5] Vierendeels, J. A., Rienslagh, K., Dick, E., and Verdonck, P. R., 2000, "Computer simulation of intraventricular flow and pressure gradients during diastole," *ASME J. Biomech. Eng.*, **122**, pp. 667–674.
- [6] Taylor, T. W., and Yamaguchi, T., 1995, "Realistic three-dimensional left ventricular ejection determined from computational fluid dynamics," *Med. Eng. Phys.*, **17**, pp. 602–608.
- [7] Jones T. N., and Metaxas D. N., 1998, "Patient-specific analysis of left ventricular blood flow," *Medical Image Computing and Computer-Assisted Intervention-MICCAI'98*, pp. 156–166.
- [8] Saber, N. R., Gosman, A. D., Wood, N. B., Kilner, P. J., Charrier, C., and Firmin, D. N., 2001, "Computational flow modelling of the left ventricle based on in vivo MRI data—initial experience," *Ann. Biomed. Eng.*, **29**, pp. 275–283.
- [9] Saber, N. R., Wood, N. B., Gosman, A. D., Yang, G. Z., Merrifield, R. D., Gatehouse, P. D., Charrier, C. L., and Firmin, D. N., 2003, "Progress towards patient-specific computational modelling of the left heart via combination of MRI with CFD," *Ann. Biomed. Eng.*, **31**, pp. 42–52.
- [10] Long, Q., Xu, X. Y., Collins, M. W., Bourne, M., and Griffith, T. M., 1998, "Magnetic resonance image processing and structured grid generation of a human abdominal bifurcation," *Comput. Methods Programs Biomed.*, **56**, pp. 249–259.
- [11] Kilner, P. J., Yang, G. Z., Wilkes, A. J., Mohiaddin, R. H., Firmin, D. N., and Yacoub, M. H., 2000, "Asymmetric redirection of flow through the heart," *Nature (London)*, **404**, pp. 759–761.
- [12] Fujimoto, S., Mohiaddin, R. H., Parker, K. H., and Gibson, D. C., 1995, "Magnetic resonance velocity mapping of normal human transmitral velocity profiles," *Heart Vessels*, **10**, 236–240.
- [13] Kim, Y. H., Walker, P. G., Pedersen, E. M., Poulsen, J. K., Oyre, S., Houliand, K., and Yoganathan, A. P., 1995, "Left ventricular blood flow patterns in normal subjects: a quantitative analysis by 3-D magnetic resonance velocity mapping," *J. Am. Coll. Cardiol.*, **26**, 224–238.

## Effect of Specimen Thickness on Fracture Toughness of Bovine Patellar Cartilage

**D. J. Adams**

Department of Orthopaedic Surgery, MC-4037,  
University of Connecticut Health Center,  
Farmington, CT 06030

**K. M. Brosche**

**J. L. Lewis\***

Department of Orthopaedic Surgery,  
University of Minnesota, Minneapolis, MN 55455

*Fracture toughness and crack tip opening angle were measured for bovine patellar cartilage using modified single-edged notch specimens of two thicknesses. There was no difference in fracture toughness between thin (0.7 mm) versus relatively thick (2.7 mm) specimens, but the crack tip opening angle at initiation of crack propagation was larger for the thin specimens (106 deg) than for the thick specimens (70 deg). Fracture toughness of the bovine patellar cartilage (1.03 kJ/m<sup>2</sup>) was not statistically different than that reported previously for canine patellar cartilage (1.07 kJ/*

*m<sup>2</sup>) employing the same methods. Large variation in measurements for both bovine and canine cartilage are in part attributable to variation between individual animals, and are consistent with variation in other mechanical property measurements for articular cartilage. The observed reduction in crack tip opening angle with increased specimen thickness is consistent with behavior of some engineering materials, and demonstrates that specimen thickness influences fracture behavior for bovine patellar cartilage.*

[DOI: 10.1115/1.1635405]

## Introduction

The strength of articular cartilage is important toward withstanding functional loads without mechanical failure or cracking. There have been extensive measurements of prefailure properties of cartilage [e.g., [1,2,3]], but few measurements of failure properties. Most testing of cartilage failure has been by one-dimensional tension testing [4,5]; however, cartilage fails by crack formation and fibrillation [6,7], suggesting that fracture toughness is a more appropriate measure of strength. Although fracture toughness is commonly measured for engineering materials [8], methods for measuring the fracture toughness of cartilage have been developed only recently and are still being improved.

Chin-Purcell and Lewis [9] measured the fracture toughness of canine patellar cartilage using a modified single edge notch (MSEN) test. Cracks were formed and propagated in the deep and mid zones, using the subchondral bone to grip the specimen. An unusual feature observed in that work was that the majority of cracks opened substantially (1–2 mm) before propagation. Although the propagation could still be monitored and a fracture parameter computed, the test did not seem to be simulating crack propagation as it occurs in vivo. In the intact joint cracks do not appear to open that wide, presumably due to the geometrical constraint provided by the surface [7]. It was speculated that one reason for the large crack opening in laboratory specimens might be due to the fact that the specimens were thin, more closely in a state of plane stress, whereas in vivo the cracks would form in a state more closely related to plane strain.

It is well known in the fracture mechanics of engineering materials that cracks in plane stress behave quite differently than cracks in plane strain [8]. Because the principal stress on the specimen surface is zero, cracks in a plane stress environment may exhibit much more plastic deformation at the crack tip and open more than cracks in plane strain conditions. Moreover, the surface region dominates the stress state whether or not significant plastic deformation occurs.

The primary goal of this study was to test the hypothesis that the fracture toughness and crack opening for articular cartilage depend on specimen thickness. A secondary goal of this study was to measure the fracture toughness of bovine patellar cartilage, a source of tissue more readily available for experimental purposes than canine cartilage. We note that our focus is a material property, not a simulation of cartilage failure.

## Materials and Methods

The procedures of Chin-Purcell and Lewis [9] were used to measure the fracture toughness of bovine patellar cartilage. Bovine patellae from 8 animals 12–18 months of age were obtained from a local abattoir. Square full-thickness 6 mm×6 mm specimens comprised of both bone and cartilage were cut from the proximal-medial region of the patellae (Fig. 1). Serial sections

\*Corresponding author: Mayo Mail Code 289; 420 Delaware St. S.E.; Minneapolis, MN 55455. Phone: 612-626-5021; Fax: 612-626-3900; e-mail: lewis001@umn.edu.

Contributed by the Bioengineering Division for publication in the JOURNAL OF BIOMECHANICAL ENGINEERING. Manuscript received December 31, 2002 by the Bioengineering Division; revision received April 22, 2003. Associate Editor: L. Sutton.

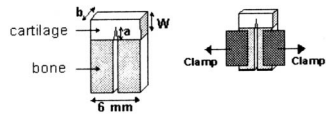


**Fig. 1 Modified single edged notch (MSEN) specimen. An initial crack is cut in the cartilage and propagated toward the surface as the load is applied parallel to the surface via clamps on the bone. Specimen geometry, overall dimension, thickness ( $b$ ) and crack length (i.e.,  $a/W$ ) are used in the calculation of fracture toughness using the analytical solution derived by Chin-Purcell and Lewis (1996).**

alternating in nominal thickness of 1 mm (thin) and 3 mm (thick) were cut in the medial-lateral direction using a diamond wafering blade. Since the surface tangential zone is stiffer than the deeper cartilage [10], 10% of the cartilage surface was removed to reduce nonuniformity in material properties. A centered cut made through the bone to separate into two supporting segments, and extended into the cartilage by cutting with a scalpel blade (Fig. 1). The resulting initial crack length,  $a$ , was limited to 5%–25% of cartilage radial depth,  $W$ , to conform within the analytical solution established for  $a/W$  by Chin-Purcell and Lewis [9]. Otherwise, variation in  $a/W$  occurred due to variation in specimen radial depth as well as our ability to create the small initial crack.

During testing the specimens were maintained in saline and pulled so as to separate the crack in Mode I. Thus the crack was initiated in the deep zone and propagated from that zone toward the articular surface. Each specimen was held using custom sandpaper-lined grips. Tensile loading was performed at a constant displacement rate of 0.2 mm/s (MicroBionix, MTS, Inc., Eden Prairie, MN). Force and actuator displacement data were collected at 10 Hz with magnified video recording of the crack opening and point of critical (initial) propagation.

Cartilage fracture toughness was measured using the J-integral method, as implemented by Chin-Purcell and Lewis for this MSEN geometry [9]. The load at which the crack started to propagate was determined using the video record. This critical load was used in an elastic stress analysis of the MSEN specimen to compute critical  $J_c$ . An equivalent elastic modulus was determined for each individual fracture test and used in the calculation of  $J_c$ , with the use of a constant loading rate justifying an elastic model. To assess critical crack opening, the included angle of the opened crack tip at the point of initial propagation was measured from a magnified video image (Fig. 2). This definition of crack tip opening (angle) is analogous to the crack tip opening displacement (CTOD) commonly used as a fracture parameter for rigid materials, here replacing mouth opening displacement with opening angle for soft tissue to obviate the dependence of crack opening on  $a/W$  and modulus.

Fracture toughness ( $J_c$ ) and crack tip opening angle (CTOA) were measured for each of 20 thin and 18 thick cartilage specimens. Statistical comparisons were performed using two-way ANOVA and Newman-Keuls test for multiple comparisons to as-

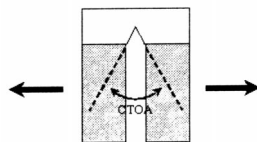


**Fig. 2 The critical crack tip opening angle (CTOA) at the onset of crack propagation was measured from a magnified video recording of each test. CTOA is analogous to the common fracture mechanics parameter of crack tip opening displacement (CTOD), but obviates the influence of tissue modulus and crack length,  $a/W$ , in the measurement of crack opening.**

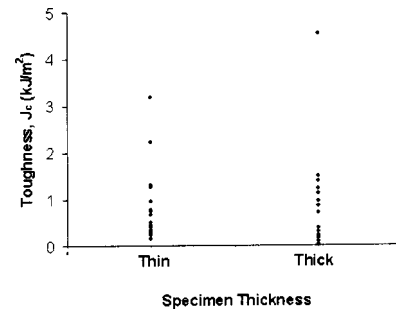


**Fig. 3 Fracture toughness ( $J_c$ ) measured in thin and thick bovine specimens demonstrated substantial variation and did not suggest a dependence on thickness.**

sess the dependence of  $J_c$  and CTOA on specimen thickness as well as the individual (bovine) animal from which each specimen was procured. To validate reproducibility of the test method for determining  $J_c$  and CTOA, and to provide comparative data for a homogeneous material, thin (0.5 mm) and thick (2.0 mm) specimens of homogeneous urethane rubber (PS-4, Measurements Group, Inc., Raleigh, NC) were bonded to rigid methacrylate (analogous to bone in the cartilage specimens) and tested in the same manner as the cartilage/bone specimens. Urethane was chosen to approximate the modulus of cartilage. CTOA was measured for thin and thick specimens and  $J_c$  was measured for thick specimens to compare to  $J_c$  data obtained by Chin-Purcell and Lewis for thick (2.0 mm) specimens of the same urethane material [9]. Standard unpaired t-tests were employed for these comparisons with a significance level of  $p=0.05$ .

## Results

The value of fracture toughness measured for the thin urethane rubber specimens was  $0.25 \pm 0.03 \text{ kJ/m}^2$ , very similar to the value of  $0.26 \pm 0.08 \text{ kJ/m}^2$  measured by Chin-Purcell and Lewis for thick specimens [9]. Crack tip opening angle in urethane specimens was not different for thin versus thick specimens ( $74 \text{ deg} \pm 9 \text{ deg}$  versus  $78 \text{ deg} \pm 9 \text{ deg}$ , respectively;  $p=0.4$ ). All cracks in urethane propagated sharply, without significant blunting at the crack tip.

In bovine cartilage, there was no statistical difference in the value of fracture toughness measured for thin versus thick specimens ( $1.05 \pm 1.59 \text{ kJ/m}^2$  versus  $0.99 \pm 1.05 \text{ kJ/m}^2$ , respectively;  $p>0.1$ , Fig. 3, Table 1). However, crack tip opening angle was significantly larger ( $p<0.0001$ ) in thin specimens ( $106 \text{ deg} \pm 20 \text{ deg}$ ) versus thick specimens ( $70 \text{ deg} \pm 18 \text{ deg}$ ). The individual (bovine) animal from which the specimen was procured demonstrated a statistically significant effect on  $J_c$  ( $p=0.008$ ), contributing to the substantial variation in measured fracture toughness.

The fracture toughness for bovine patella cartilage was compared to the value of fracture toughness for canine patellar carti-

**Table 1 Fracture toughness ( $J_c$ ) and crack tip opening angle for bovine patella cartilage**

	Fracture Toughness <sup>(1)</sup> (KJ/m <sup>2</sup> )	Crack Tip Opening Angle (Degrees)
Thin (N=20)	$1.05 \pm 1.59$	$106 \pm 20$
Thick (N=18)	$0.99 \pm 1.05$	$70 \pm 18$ <sup>(2)</sup>
All (N=38)	$1.03 \pm 1.09$	
Canine (N=87)	$1.07 \pm 0.87$	N/A <sup>(3)</sup>

<sup>(1)</sup>There was no statistically significant difference in fracture toughness between any of the categories.

<sup>(2)</sup>Statistically different between thin, thick at  $p<0.0001$ .

<sup>(3)</sup>Crack opening in the previous study of thin canine specimens demonstrated a broad range and was assessed qualitatively by category rather than quantitatively.

lage from Chin-Purcell and Lewis [9]. From this comparison, there was no statistical difference in the fracture toughness obtained for bovine and canine cartilage.

The average equivalent elastic modulus for all bovine cartilage specimens was 10.7 MPa, within the range of 5–25 MPa reported for the tensile modulus of cartilage [10]. The average elastic modulus computed for the urethane rubber was 3.9 MPa, close to the manufacturer's specified value of 4.0 MPa.

## Discussion

The primary goal of this study was to test the hypothesis that fracture toughness and initial crack propagation opening angle of articular cartilage depend on specimen thickness as measured in these experiments. Crack opening did depend on specimen thickness, confirming speculation that this could be one reason that thin specimens used by Chin-Purcell and Lewis [9] opened to what seemed an unrealistic magnitude before the cracks propagated. The crack opening measured for moderately thicker specimens remains large in comparison to that which apparently occurs in articular surfaces, as the thick specimens are not a direct simulation of the geometrical constraint provided by the intact articular surface.

Fracture toughness itself did not appear to be affected by specimen thickness. Therefore, the greater crack opening suggests that the larger elastic deformation occurring within thin specimens does not alter fracture mechanisms. However, since crack opening is often used as a fracture outcome parameter in engineering fracture mechanics, the importance of specimen thickness in crack propagation behavior for cartilage should be considered in future fracture tests. The lack of thickness dependence on crack opening in urethane is consistent with the observation that cracks remain sharp and propagate without appreciable crack tip plasticity in that material.

In this study, radial cracks were initiated in the deep to middle zone of the cartilage and propagated toward the articular surface, whereas articular cracks form *in vivo* within the surface zone and propagate inward. Fracture behavior within the surface zone certainly would be different than for the deeper zones, with orientation of collagen fibers tangential to the surface rather than radial. The effect of which direction the crack is driven (i.e., radially outward versus inward) was presumably minimized by measuring a critical value for fracture toughness and crack opening at the instant of propagation.

The secondary goal of this study was to determine the fracture toughness of bovine cartilage. Bovine cartilage is readily available for *in vitro* testing, providing a more convenient *in vitro* cartilage model than canine tissue, the only tissue for which a fracture toughness value was available. There was no difference between the canine and bovine cartilage fracture toughness measured by the MSEN method, although both species demonstrated substantial variation in fracture toughness (Fig. 3).

The variation in fracture toughness measured for bovine specimens was large, with a standard deviation of the same magnitude as the mean value (i.e., 100% variation). By comparison, reported variation in prefailure material properties is on the order of 20%–50% [3]. Chin-Purcell and Lewis documented an influence of the individual animal (canine) and location on the patella from which specimens were procured as factors affecting fracture toughness [9]. Variation between individual animals (bovine) also affected fracture toughness in the present study. In the canine study a large

range of crack opening behavior was documented, with some specimens opening little before crack propagation and some opening widely and not propagating at all [9]. This variation in crack propagation behavior suggested true differences in material properties between specimens. However, neither proteoglycan nor collagen concentration correlated with crack opening behavior in the canine study [11], suggesting that some other characteristic of the tissue was responsible for the observed differences. As these are the first studies to quantify cartilage fracture toughness, the specific factors influencing fracture toughness and crack propagation in cartilage are unknown. There are other limitations in the test methods, which are another source of the variations. Assuming an isotropic elastic material is surely an approximation. Large deformations may play a role as well. See [9] for a discussion of potential experimental error sources.

## Conclusions

For the two cartilage specimen thicknesses tested, crack tip opening angle was influenced by thickness in a MSEN fracture test of cartilage, while fracture toughness was not. Cracks opened less for thicker specimens than for thinner specimens, a factor that should be considered in fracture tests of cartilage. Fracture toughness ( $J_c$ ) of bovine patella cartilage was 1.03 kJ/m<sup>2</sup>, a value similar to that reported for canine patella cartilage.

## Acknowledgments

This work was supported by the Catharine Mills Davis Endowment to the Department of Orthopaedic Surgery at the University of Minnesota, a Research Initiation grant from the University of Connecticut Health Center, the Arthritis Foundation, NIH grant AR41975, and the MRSEC Program of the National Science Foundation under Award Number DMR-9809364. The authors thank Mary Slagle for assistance in testing.

## References

- [1] Kempson, G. E., 1979, "Mechanical properties of articular cartilage." In Freeman, M.A.R. (ed): *Adult Articular Cartilage*, ed 2. Kent, UK, Pitman Medical Publishers, pp. 333–414.
- [2] Mow, V. C., Ateshian, G. A., and Spilker, R. L., 1993, "Biomechanics of diarthrodial joints: A review of twenty years of progress." *J. Biomech. Eng.*, **115**, pp. 460–467.
- [3] Mow, V. C. and Radcliffe, A., 1997, "Structure and function of articular cartilage and meniscus." In Mow, V. C. and Hayes, W. C., *Basic Orthopaedic Biomechanics*, ed 2. Philadelphia, PA, Lippincott-Raven Press, pp. 113–177.
- [4] Roberts, S., Weightman, B., Urban, J., Chappell, D., 1986, "Mechanical and biochemical properties of human articular cartilage in osteoarthritic femoral heads and in autopsy specimens." *J. Bone Jt. Surg.*, **68B**, pp. 278–288.
- [5] Schmidt, M. B., Mow, V. C., Chun, L. E., and Eyre, D. R., 1990, "Effects of proteoglycan extraction on the tensile behavior of articular cartilage." *J. Orthop. Res.*, **8**, 353–363.
- [6] Clark, J. M., and Simonian, P. T., 1997, "Scanning electron microscopy of 'fibrillated' and 'malacic' human articular cartilage: technical considerations." *Microsc. Res. Tech.*, **37**, pp. 299–313.
- [7] Lewis, J. L., and Johnson, S. L., 2001, "Collagen architecture and failure processes in bovine patellar cartilage." *Journal of Anatomy*, **199**, pp. 483–492.
- [8] Atkins, A. G. and Mai, Y. W., 1985, *Elastic and Plastic Fracture: Metals, Polymers, Ceramics, Composites, Biological Materials*. Ellis Horwood Ltd., Chichester and John Wiley and Sons, N.Y.
- [9] Chin-Purcell, M. V., and Lewis, J. L., 1996, "Fracture of Articular Cartilage." *J. Biomech. Eng.*, **118**, pp. 545–556.
- [10] Elliot, D. M., Narmoneva, D. A., and Setton, L. A., 2002, "Direct Measurement of the Poisson's Ratio of Human Patella Cartilage in Tension." *J. Biomech. Eng.*, **124**, pp. 223–228.
- [11] Chin-Purcell, M., 1995, *Fracture Toughness of Cartilage*, Ph.D. Dissertation, University of Minnesota.